EVOLUTION OF THE BOLOMETRIC TEMPERATURE AND LUMINOSITY OF YOUNG STELLAR OBJECTS

P. C. MYERS,[1] F. C. ADAMS,[2] H. CHEN,[1,3] AND E. SCHAFF[2]

ABSTRACT

We model the broadband emission from a star-disk-envelope system to obtain expressions for the bolometric temperature T_{bol} and luminosity L_{bol} as functions of time, from the youngest class 0 protostars to stars on the zero-age main sequence. The model predicts evolution, driven by infall and contraction luminosity, in terms of position on the log T_{bol}–log L_{bol} diagram, a close analog of the H-R diagram. The evolutionary tracks depend on the envelope initial conditions, the main-sequence mass of the star, and the envelope dissipation timescale. The model L_{bol} rises due to infall and then falls due to contraction, while T_{bol} increases steadily toward the main sequence due to central heating and envelope dissipation. In order to smoothly join the protostellar and pre–main-sequence phases it is necessary to model the termination of infall as gradual rather than sudden. This change reduces the peak infall luminosity for the collapse of a singular isothermal sphere by a factor 4, bringing predicted infall luminosities into better agreement with observations. For stars of main-sequence mass 0.5 $M_\odot$, the model decrease in L_{bol} from its peak value of ~ 3 $L_\odot$ at $T_{bol} \sim 250$ K (class I) to ~ 0.4 $L_\odot$ at $T_{bol} \sim 3000$ K (class II/III) closely matches the observed decrease in median L_{bol} for young stellar objects in Chamaeleon, Corona Australis, Lupus, Ophiuchus, and Taurus. The model should be useful for estimating the distributions of mass and age, and for describing the birth history, of stars younger than 1 Myr in well-studied complexes.

Subject headings: stars: evolution — stars: fundamental parameters — stars: pre–main-sequence

1. INTRODUCTION

The Hertzsprung-Russell (H-R) diagram (Hertzsprung 1905; Russell 1914) is the outstanding example of the use of stellar properties derived from optical observations to classify and distinguish groups of stars. Since the development of nuclear astrophysics, the H-R diagram has also become the main way to describe stellar evolution (e.g., Schwarzschild 1958) and pre–main-sequence evolution (Levee 1953; Henyey, LeLevier, & Levee 1995; Hayashi, Hoshi, & Sugimoto 1962). These stellar evolution models, and their refinements (Iben 1965; D'Antona & Mazzitelli 1994, hereafter DM) have been widely used to infer the masses and ages of stars from their positions on the H-R diagram.

The H-R diagram cannot be used to describe the earliest phases of star formation because then the typical young stellar object (YSO) does not possess a well-defined photosphere, an optically thick surface radiating as a blackbody at a constant temperature T_{eff} of several thousand K. Instead, much of its luminosity emerges at submillimeter, far-infrared, and near-infrared wavelengths. It spectrum is much broader than a blackbody and arises from gas and dust with a wide range of temperature colder than T_{eff} (Beichman et al. 1986).

Comparison of YSO spectra and molecular line maps in the nearest star-forming regions indicate that sources with redder broadband spectra are more frequently associated with dense cores of gas and dust (Lada & Wilking 1984; Myers et al. 1987). This tendency is widely attributed to "spectral evolution," where the youngest YSOs are surrounded by envelopes optically thick at all but the longest wavelengths, in the far-infrared and submillimeter. As circumstellar matter dissipates, due probably to a combination of infall and outflow, the effective optical depth decreases, and the spectrum evolves toward the blue, resulting in an optically visible pre–main-sequence star with an associated circumstellar disk (Adams, Lada, & Shu 1987, hereafter ALS).

Many ways have been proposed to quantify the spectral color of YSOs. The best-known scheme distinguishes the spectral classes I, II, and III according to the slope between near-infrared and mid-infrared emission on a log-log plot of the spectral energy distribution (Lada & Wilking 1984; Lada 1987). The reddest "class 0" sources are distinguished by their high proportion of luminosity at submillimeter wavelengths (André, Ward-Thompson, & Barsony 1993). Another evolutionary diagram uses the bolometric luminosity L_{bol} and the observed millimeter wavelength flux as its two axes (Saraceno et al. 1996a, 1996b).

In this paper we quantify spectral redness with the "bolometric temperature," the temperature of a blackbody whose spectrum has the same mean frequency $\langle v \rangle$ (Ladd et al. 1991) as the observed spectrum:

$$T_{bol} = \frac{\zeta(4)}{4\zeta(5)} \frac{h\langle v \rangle}{k} = 1.25 \times 10^{-11} \langle v \rangle \text{ K Hz}^{-1}$$

(Myers & Ladd 1993, hereafter ML). This description is closely related to the H-R diagram because a log-log plot of bolometric luminosity versus bolometric temperature ("BLT diagram") has the same main sequence as the H-R diagram. In this diagram, spectral evolution proceeds toward the main sequence from low (~ 30 K) to high (~ 3000 K) values of T_{bol}.

[1] Harvard-Smithsonian Center for Astrophysics, 60 Garden Street, Cambridge, MA 02138.
[2] Department of Physics, University of Michigan, Ann Arbor, MI 48109.
[3] Steward Observatory, University of Arizona, Tucson, AZ 85721.

BLT diagrams of star-forming complexes differ in the proportion of YSOs with low and high values of T_{bol} in Taurus and Ophiuchus (Chen et al. 1995), and in Lupus Chamaeleon, and Corona Australis (Chen et al. 1997). Regions dominated by young clusters (Corona Australis and Ophiuchus) also have a much greater proportion of YSOs with low values of T_{bol}. This result suggests that the BLT diagram can distinguish regions with different star formation histories.

Another related method that has been proposed to study protostellar evolution is the luminosity versus visual extinction (L-A_V) diagram (Adams 1990). In this approach, the visual extinction A_V is a measure of the total optical depth of the infalling protostellar envelope and thus characterizes YSOs during the infall phase. During this infall phase, the visual extinction is well correlated with the bolometric temperature T_{bol} used here (see the Appendix) so that these two diagrams are analogous for this phase of evolution. Similarly, for revealed stellar sources, the bolometric temperature used here becomes equivalent to the usual photospheric temperature, and the BLT diagram thus is equivalent to the H-R diagram in this limit. The advantage of our present approach (the BLT diagram) is that it smoothly connects the embedded protostellar phase with the later (optically revealed) stellar phases in a single diagram. In other words, the BLR diagram can be used to simultaneously consider both deeply embedded protostellar objects and fully revealed PMS stars.

A better understanding of how YSO spectra evolve requires comparison of observations with models. In this paper we present simple models of YSO spectra which depend on the initial properties of the parent dense core and on time since the start of infall. The purpose of these models is to take the first step toward a framework for interpretation of YSO properties from their position on the BLT diagram. The models are neither unique nor completely self-consistent, but we believe they present several essential features of spectral evolution of YSOs.

The basic model consists of a star, an optically thick disk, and a spherical envelope. The luminosity increases due to dynamical infall and then decreases due to quasi-static contraction. The envelope mass, optical depth, and infall onto the star-disk system are constant at early times but decrease gradually at late times. The temperature T_{bol} increases monotonically with time due to increasing heating at early times and to decreasing optical depth at late times.

This paper is organized as follows. Sections 2 and 3 describe the basic properties of the model. Section 4 gives the results of model calculations for various choices of core parameters, compares predicted and observed distributions of YSOs, and addresses departures from a spherically symmetric envelope. Section 5 presents a summary and discussion. The Appendix compares model predictions and numerical calculations for the protostellar phase.

2. THE MODEL

The model is intended to be the simplest possible which incorporates the radiative transfer associated with idealized versions of a star, disk, and envelope, and which gives analytic expressions for the bolometric temperature and luminosity in terms of the stellar mass, time, and dense core temperature. The model predicts the two lowest moments of the YSO spectrum, not its detailed spectral shape. To achieve the goal of analytic simplicity it is necessary to sacrifice some realism in treating the system components. For example, the disk is smaller than a centrifugally supported accretion disk, for some parameter values, as explained in § 2.4.

The model is described in two parts. The first part, § 2, gives the radiative transfer relations needed to express the bolometric temperature T_{bol} and the ratio of stellar luminosity to envelope mass $L_\star/M_e$ in terms of the optical depth. The second part, § 3, relates to the ratio $L_\star/M_e$ to the luminosity and to the time since the start of gravitational infall.

2.1. The System

The geometry of the star-disk-envelope system is shown in Figure 1. The star and envelope have concentric spherical symmetry, and the disk has cylindrical symmetry about an axis passing through the center of the star. The stellar luminosity $L_\star$ is the sole source of luminosity for both the disk and the envelope, so $L_\star$ equals L_{bol}, the bolometric luminosity of the
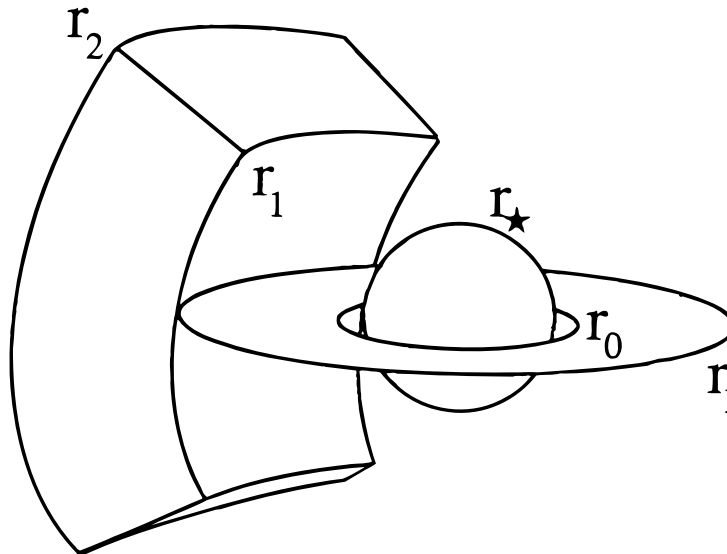

FIG. 1.—Sketch of model star, disk, and a section of the spherical envelope, labeled with their radii $r_\star$, r_0, r_1, and r_2. The sketch is not drawn to scale.

system. The disk absorbs and reradiates a fraction f of the stellar luminosity, and the envelope absorbs and reradiates a fraction g of the stellar luminosity, part directly from the star and the remainder from the disk.

2.2. The Star

The star has a blackbody photosphere with radius $r_\star$, temperature $T_\star$, and luminosity $L_\star = 4\pi r_\star^2 \sigma T_\star^4$, where σ is the Stefan-Boltzmann constant. The luminosity $L_\star$ is the sum of both "infall" luminosity L_{in}, which dominates the protostar phase, and "contraction" luminosity L_{con}, which dominates the pre–main-sequence phase. The contraction luminosity L_{con} and stellar effective temperature $T_\star$ for a given stellar mass and age are taken from D'Antona & Mazzitelli (1994) Tables 1 and 5, for "CM Alexander" opacity and convection. We note that the label "con" refers to both gravitational contraction and deuterium burning, as calculated by D'Antona & Mazzitelli. The infall luminosity is based on a modification of the collapse of a singular isothermal sphere (Shu 1977), described in § 3.

2.3. The Disk

The disk is geometrically thin and optically thick at all wavelengths, with inner radius and temperature r_0 and T_0, outer radius and temperature r_1 and T_1, and temperature law

$$T(r_d) = T_0(r_d/r_0)^{-1/2} = T_1(r_d/r_1)^{-1/2} \, , \tag{1}$$

for disk radius r_d in the range $r_0 \le r_d \le r_1$. This temperature law is flatter than expected for viscous accretion, where $T \sim r^{-3/4}$ (e.g., Lynden-Bell & Pringle 1974) but is closer to that needed to account for the broadband spectra of many "flat-spectrum" T Tauri stars (ALS; see also § 2.5 below). The specific luminosity of the disk is obtained by integrating the blackbody emission over the disk, yielding

$$L_{v,d} = \frac{8\pi r_0^2 T_0^4 \sigma}{v} \frac{\int_{x_{min}}^{x_{max}} dx \, x^3(e^x - 1)^{-1}}{\int_0^\infty dx \, x^3(e^x - 1)^{-1}} \, , \tag{2}$$

where $x \equiv hv/kT$, $x_{min} = hv/kT_0$, and $x_{max} = hv/kT_1$. The corresponding bolometric luminosity and temperature are then obtained from the zeroth and first moments of equation (2) (ML):

$$L_d = 8\pi r_0^2 T_0^4 \sigma \ln(T_0/T_1) \, , \tag{3}$$

$$T_{bol,d} = (T_0 - T_1)/\ln(T_0/T_1) \, . \tag{4}$$

The maximum disk temperature T_0 is taken to be 1500 K, the dust destruction temperature of graphite (e.g., Adams & Shu 1985). The minimum disk temperature T_1 is set by luminosity conservation between star, disk, and envelope, as explained below.

If the temperature law were $T \sim r^{-3/4}$ (e.g., Beckwith et al. 1990), equation (3) for L_d and equation (4) for $T_{bol,d}$ would change. For temperature of the disk outer edge, 1000 K $< T_1 <$ 1500 K, $L_d(3/4) \approx 0.7 L_d(1/2)$, while $T_{bol,d}(3/4) \approx 1.1 T_{bol,d}(1/2)$. For colder and larger disks, with T_1 decreasing to 100 K, $L_d(3/4)/L_d(1/2)$ decreases to about 0.2, while $T_{bol,d}(3/4)/T_{bol,d}(1/2)$ increases to about 1.6. These changes have their greatest effect when considering the disk contributions alone. When stellar emission and envelope reprocessing are included, these changes in disk temperature law are generally unimportant to the L_{bol} and T_{bol} of the system. The greatest change for the system occurs in the T Tauri phase when the envelope is optically thin.

2.4. The Envelope

In our simple model, the spherically symmetric envelope is assumed to have inner radius equal to the disk outer radius r_1, inner temperature equal to the disk outer temperature T_1, and inner density ρ_1. In the collapse calculations of the singular isothermal sphere, rotation leads to an angular momentum barrier which presents much of the infalling material from falling to the stellar surface (e.g., Terebey, Shu, & Cassen 1984). This centrifugal barrier thus provides an effective inner boundary of the envelope and defines the outer edge of the circumstellar disk. Although some infalling material does fall inside this radius, we ignore this effect in our simple model and use a well defined inner boundary to the envelope.

We also assume that the envelope has an effective outer boundary, denoted here as r_2. This outer boundary defines the effective sphere of influence of the protostar. We stress that this boundary is not a physical boundary within the molecular cloud, which is far more extended. The corresponding temperature and density are denoted T_2 and ρ_2. We take T_2 to be the temperature where the centrally heated envelope merges into the more uniform background, generally close to 10 K. The envelope density is assumed to depend on radius r as

$$\rho(r) = \rho_1(r/r_1)^{-3/2} = \rho_2(r/r_2)^{-3/2} \, , \tag{5}$$

for r in the range $r_1 \le r \le r_2$. This density law exponent, $-3/2$, is expected for gravitationally infalling gas in the outer regime (e.g., Shu 1977) and is similar to that derived from observations of low-mass dense cores (e.g., Fuller & Myers 1992). The corresponding envelope mass is then given by

$$M_e = \frac{8\pi}{3} \rho_1 r_1^{3/2}(r_2^{3/2} - r_1^{3/2}) \, . \tag{6}$$

Similarly, the envelope optical depth from r to r_2 is

$$\tau = 2\kappa\rho_1 r_1^{3/2}(r^{-1/2} - r_2^{-1/2}) \, , \tag{7}$$

where κ is the dust emissivity. We denote the optical depth from r_1 to r_2 as τ_{12}. To keep the analysis simple we assume that the emissivity follows a single power law with frequency v, $\kappa = Av$, where $A = 1.59 \times 10^{-13}$ cm^2 g^{-1} Hz^{-1}. This value of A was chosen so that the resulting curve passes through the more detailed emissivity profile of Draine & Lee (1984; see also Adams & Shu 1985) at the near-infrared, mid-infrared, and far-infrared wavelengths of 2, 12, and 60 μm. We take 12 μm to be a fiducial wavelength, and we call the corresponding emissivity κ_{IR} and the corresponding total optical depth τ_{IR}.

2.4.1. Optically Thick Envelope

The radiative transfer in the envelope is evaluated in two approximations: optically "thick" when $\tau_{IR} > \tau_0$, and "thin" when $\tau_{IR} < \tau_0$. Here $\tau_0 < 1$, and its exact value is chosen to minimize the difference in the ratio $L_\star/M_e$ between the approximations.

We model the optically thick emission using a "photospheric" approximation similar to that of Kenyon, Calvet, & Hartmann (1993). The emission at each frequency v is that of a blackbody with radius $r_{\tau=1}$ that is the radius of unit optical depth:

$$L_{v,e,\text{thick}} = 4\pi^2 r_{\tau=1}^2 B_v[T(r_{\tau=1})] , \tag{8}$$

where B_v is the Planck function. We obtain $r_{\tau=1}$ by setting $\tau = 1$ in equation (7) and by assuming that the ratio of envelope and disk sizes is large, i.e., $r_2/r_1 \gg \tau_{12}^2$. This assumption yields $r_{\tau=1} \approx r_1 \tau_{12}^2$. The corresponding temperature is $T_{\text{thick}}[r_{\tau=1}] \approx T_{1,\text{thick}}/\tau_{12}$ according to the temperature law

$$T_{\text{thick}} = T_{1,\text{thick}}(r/r_1)^{-1/2} . \tag{9}$$

This temperature law exponent, $-\frac{1}{2}$, can be shown to be necessary in this approximation because it is the only value for which the luminosity is conserved, independent of optical depth. Then L_v can be written

$$L_{v,e,\text{thick}} = \frac{8\pi^2 r_1^2 h\tau_{12}^4 v^3}{c^2} \left[\exp\left(\frac{\tau_{12} hv}{kT_1}\right) - 1 \right]^{-1} , \tag{10}$$

where τ_{12} is the optical depth between r_1 and r_2, and is linear in frequency v. This function is narrower than a blackbody but still provides a reasonable estimate of the mean frequency, and thus of T_{bol}. Then integration of equation (10) yields the envelope luminosity and bolometric temperature

$$L_{e,\text{thick}} = 2\pi\sigma r_1^2 T_{1,\text{thick}}^4 , \tag{11}$$

$$T_{\text{bol},e,\text{thick}} = \left(\frac{h\kappa_{IR} T_{1,\text{thick}}}{kA\tau_{IR}}\right)^{1/2} \frac{\Gamma(9/2)\zeta(9/2)}{\Gamma(5)\zeta(5)} , \tag{12}$$

Here the envelope luminosity is independent of optical depth, but the bolometric temperature decreases with increasing τ_{IR}, as $\tau_{IR}^{-1/2}$, in the sense expected for a centrally heated photosphere.

The envelope absorbs and reradiates a fraction g of the luminosity from the star-disk system, so that $L_{e,\text{thick}} = gL_\star$. Then we combine the definition of $f = L_d/L_\star$ with equations (3), (9), and (11) to obtain the disk-envelope boundary temperature $T_{1,\text{thick}}$ in terms of f, g, and the disk inner temperature T_0,

$$T_{1,\text{thick}} = T_0 \exp\left(-f/4g\right) . \tag{13}$$

Note that $T_{1,\text{thick}}$ is sensitive to f/g. If the envelope is optically thick to the star-disk emission in all directions, then $g = 1$, so for $T_0 = 1500$ K and $f = \frac{1}{4}$, $T_{1,\text{thick}} \approx 1100$ K. For $L_\star = 1 L_\odot$ the corresponding disk radius, from equation (11), is only 0.1 AU. This small disk is an unrealistic consequence of the purely spherical geometry, but for the optically thick envelope the disk emission is fully reprocessed, so this small disk size has no effect on the emergent envelope spectrum. On the other hand, if the envelope has polar holes or is optically thin over a significant solid angle, so that $g = 0.01$, then $T_{1,\text{thick}} = 17$ K and $r_1 = 74$ AU, consistent with a rotating accretion disk.

The ratio of stellar luminosity to envelope mass in the optically thick approximation is now specified in terms of the optical depth and the envelope boundary temperatures $T_{1,\text{thick}}$ and T_2, using equations (6), (7), (9), and (11):

$$\left(\frac{L_\star}{M_e}\right)_{\text{thick}} = \frac{3\sigma\kappa_{IR} T_2^3 T_{1,\text{thick}}}{2\tau_{IR}} . \tag{14}$$

2.4.2. Optically Thin Envelope

For an optically thin envelope with opacity law $\kappa = Av$, heated by a central source of luminosity $L_\star$, the temperature decreases with radius r_e as

$$T_{\text{thin}} = B(gL_\star)^{1/5} r_e^{-2/5} , \tag{15}$$

where g is the fraction of $L_\star$ absorbed by the envelope, and where the coefficient B is given by

$$B = \left[\frac{\kappa_E h}{16\pi\sigma kA} \frac{\Gamma(4)\zeta(4)}{\Gamma(5)\zeta(5)}\right]^{1/5} , \tag{16}$$

with κ_E the energy-weighted mean opacity (Adams 1991), for which we adopt $\kappa_E = 6$ cm^2 g^{-1} for the envelope temperature range of interest (see Adams 1988, Fig. 2.2).

With the temperature law in equation (15), we obtain the specific luminosity of the optically thin envelope in the form

$$L_{v,e,\text{thin}} = \frac{600}{\pi^3} \sigma A \rho_1 r_1^3 T_{1,\text{thin}}^4 \left(\frac{hv}{kT_{1,\text{thin}}}\right)^{1/4} \int_{x_{\min}}^{x_{\max}} dx \, x^{11/4} (e^x - 1)^{-1} , \tag{17}$$

where now $x_{\min} = hv/kT_2$ and $x_{\max} = hv/kT_{1,\text{thin}}$, Integrating over frequency yields the bolometric luminosity and temperature, assuming $T_{1,\text{thin}} \gg T_2$:

$$L_{e,\text{thin}} = \frac{2\kappa_E \rho_1 r_1^3 T_{1,\text{thin}}^5}{B^5} , \tag{18}$$

$$T_{\text{bol},e,\text{thin}} = \left(\frac{5}{6}\right)^2 \frac{\zeta(4)\zeta(6)}{\zeta^2(5)} T_{1,\text{thin}} . \tag{19}$$

Equating expressions for disk luminosity, using equations (1), (3), and (15), we obtain the temperature $T_{1,\text{thin}}$:

$$\frac{T_{1,\text{thin}}}{\ln(T_0/T_{1,\text{thin}})} = \frac{8\pi\sigma B^5 g}{f} . \tag{20}$$

As in the case of the optically thick envelope $T_{1,\text{thin}}$ depends on the ratio of the disk and envelope interception factors f/g. For the standard disk interception factor $f = \frac{1}{4}$ and the envelope factor $g = 0.01$ considered above, $T_{1,\text{thin}} = 35$ K. For $L_\star = 1 \, L_\odot$, equation (15) gives $r_1 = 23$ AU. As f decreases, r_1 decreases and $T_{1,\text{thin}}$ increases.

Combining equations (6), (7), (15), (18), and (20) gives the ratio of stellar luminosity to envelope mass in the optically thin approximation:

$$\left(\frac{L_\star}{M_e}\right)_{\text{thin}} = \frac{3\kappa_{\text{IR}} T_2^{15/4} T_{1,\text{thin}}^{5/4}}{4\pi B^5 \tau_{\text{IR}}} . \tag{21}$$

2.5. Interception Factors

The star-disk interception factor f is modeled as increasing smoothly from 0 to 1 with increasing optical depth τ_{IR}, in accord with the tendency for infrared excess, an indicator of disk mass and extent, to correlate with molecular emission, an indicator of envelope mass and extent (Beichman et al. 1986). For a perfectly thin disk of infinite extent, $f = \frac{1}{4}$ (Adams & Shu 1986). We take this case to correspond to $\tau_{\text{IR}} \approx 1$. For greater values of τ_{IR} we assume that f increases toward 1. Thus we take

$$f = \left[1 - \exp\left(-\frac{\tau_{\text{IR}}}{\tau_a}\right)\right] \frac{1 - \exp(-\tau_{\text{IR}}/4\tau_b)}{1 - \exp(-\tau_{\text{IR}}/\tau_b)} , \tag{22}$$

where τ_a sets the transition from $f = 0$ to $f = \frac{1}{4}$, and τ_b sets the transition from $f = \frac{1}{4}$ to $f = 1$. We adopt $\tau_a = 1$ and $\tau_b = 3$. The results in § 3 are relatively insensitive to τ_a and τ_b. The adopted upper limit on f was chosen for convenience to be 1, and thus is greater than the maximum value of "backwarming," $\frac{5}{8}$, estimated by Natta (1993). However, for the high envelope optical depths where $f > \frac{5}{8}$, the optically thick expressions in § 2.4.1 for envelope bolometric temperature and luminosity indicate that as $f_{\max}$ decreases from 1 to $\frac{5}{8}$, T_{bol} increases by only 5% and L_{bol} increases by only 10%. These changes are small compared to other model uncertainties, and so can be neglected.

The fraction g of the stellar luminosity absorbed by the envelope can be written from luminosity conservation as

$$g = 1 - (1 - f)h_\star - f h_d , \tag{23}$$

where $h_\star$ is the fraction of the stellar luminosity, not absorbed by the disk, which is transmitted by the envelope and where h_d is the fraction of the stellar luminosity, absorbed and reradiated by the disk, which is transmitted by the envelope.

We approximate the envelope transmission of the disk emission by $h_d = \exp(-\tau_{\text{IR}})$ since most of the disk emission emerges at near- and mid-infrared wavelengths. For the low optical depths where h_d is important, $h_d \approx 1 - \tau_{\text{IR}}$. In this case a more exact but less convenient estimate of h_d is easily shown to be $h_d' = 1 - \tau_{1,2}(\langle v \rangle_d)$, where $\tau_{1,2}(\langle v \rangle_d)$ is the envelope optical depth at the mean frequency of the disk spectrum. These two expressions differ slightly: for $\tau_{\text{IR}} = 0.05$ and $T_{1,\text{thin}} = 1000$ K, $h_d = 0.95$ while $h_d' = 0.89$. Therefore, we use the more convenient h_d rather than h_d'. Similarly, we obtain $h_\star$ by taking the characteristic wavelength of the stellar emission to be 1 μm, so that $h_\star = \exp(-\tau_{\text{IR}}/12)$.

2.6. Bolometric Temperatures of the Star-Disk-Envelope System

The foregoing results are now combined to give expressions for the bolometric temperature of the star-disk-envelope system in the thick and thin approximations:

$$T_{\text{bol,thick}} = T_{\text{bol},e,\text{thick}} , \tag{24a}$$

$$T_{\text{bol,thin}} = T_\star (1 - f)h_\star + T_{\text{bol},d} f h_d + g T_{\text{bol},e,\text{thin}} . \tag{24b}$$

Thus in the thick approximation the T_{bol} of the system is just the T_{bol} of the envelope since the spectrum of the hotter interior is completely absorbed and reradiated. In the thin approximation each of the three components—star, disk, and envelope— contributes its individual value of T_{bol}, weighted by the product of two factors: the fraction of the stellar luminosity which it emits (respectively 1, f, and g), and the fraction of this emission which emerges without reprocessing from the outer boundary

of the envelope [respectively $(1 - f)h_\star$, h_d, and 1]. When the envelope is optically thin, it absorbs relatively little of the stellar and disk emission, so $T_{bol,thin}$ lies between $T_\star$ and $T_{bol,d}$.

2.7. Relations among L/M_e, τ_{IR}, and T_{bol}

Sections 2.1–2.6 develop expressions for $T_{bol}(\tau_{IR})$ and $L_\star/M_e(\tau_{IR})$ in optically thick and thin approximations. These relations are illustrated in Figure 2. Notice that the optical depth τ_{IR} spans several orders of magnitude during the course of YSO evolution (Adams 1990). We denote as τ_0 the value of τ_{IR} where the approximation switches from thick to thin. As τ_{IR} decreases from optically thick values, T_{bol} increases as $\tau_{IR}^{-1/2}$ and $L_\star/M_e$ increases as τ_{IR}^{-1}. At $\tau_{IR} = \tau_0$ both T_{bol} and $L_\star/M_e$ change discontinuously, by a factor of order 2. We choose τ_0 to minimize this discontinuity. This discontinuity between the thick and thin approximations is not crucial to the main results, as will be seen in § 4. Then T_{bol} levels off to the stellar temperature, while $L_\star/M_e$ increases as $\tau_{IR}^{-5/4}$. Variation of the parameters A, κ_E, κ_{IR}, and T_2 over plausible ranges changes the values of T_{bol} and $L_\star/M_e$ by amounts small compared to their variation over the likely range of several decades in τ_{IR}.

2.8. Limitations of the Model Geometry

The model geometry assumed here is limiting because the envelope has spherical symmetry and thus has the same optical depth at the poles as at the equator. When Adams & Shu (1985) modeled protostar spectra with a purely spherical envelope the resulting spectra were narrower than the observed spectral width of class I sources. They overcame this problem by adopting the nonspherical envelope structure of Terebey et al. (1984) expected for a rotating, collapsing system with a disk (Adams & Shu 1986). This geometry allows the wide range of frequencies emitted by the disk to emerge from the polar latitudes, where the envelope is less opaque than at equatorial latitudes. In the present treatment with a purely spherical envelope, the model spectra are also narrower than observed, as discussed in § 2.4.1. This discrepancy is much less important than it was for Adams & Shu (1985, 1986) because our model spectra are used only to obtain the luminosity and mean frequency, not the detailed spectral shape. The mean frequencies of the present model and of Adams & Shu (1986) agree well for class I sources, as shown in the Appendix.

On the other hand, our use of a purely spherical envelope, which starts at the same radius where the disk ends, implies that the disk inner and outer temperatures can differ by a relatively small geometrical factor, when the interception factors f and g are comparable (cf. eqs [13], [20]). In turn, this implies that the disk outer radius can be much smaller than the 100 AU expected for a rotating accretion disk, as discussed in § 2.4.
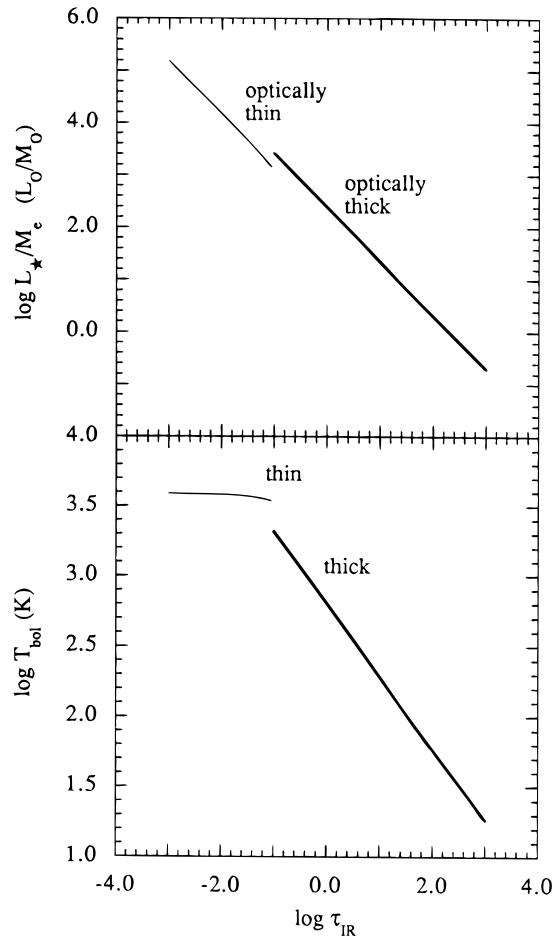

FIG. 2.—Curves of $L_\star/M_e$, the ratio of stellar luminosity to envelope mass (top), and of T_{bol}, the bolometric temperature (bottom), vs. envelope optical depth at 12 μm, τ_{IR}, in the optically thick approximation (heavy lines), and in the optically thin approximation (light lines).

This difference in disk size is important for detailed comparisons of disk and envelope spectra, but it does not significantly limit the model predictions of T_{bol} for the combined star-disk-envelope system. For class 0 and early class I sources, the disk emission is completely reprocessed by the optically thick envelope for either disk size. For late class I sources, for class II and III sources, the envelope becomes optically thin to the disk emission but still has significant optical depth to the shorter wavelength stellar flux. Thus the envelope absorbs and reprocesses enough of the stellar flux to provide values of T_{bol} corresponding to the observed infrared excess, as will be seen in §§ 4.3 and 4.4. The present treatment should be improved in future versions, possibly by allowing the disk to extend into the envelope, or by reducing the envelope optical depth with increasing latitude, as was done by Adams & Shu (1986).

3. ENVELOPE DISSIPATION AND LUMINOSITY EVOLUTION

To predict the variation of $L_\star$ and T_{bol} with time t from the relations in § 2 it is necessary to specify how $L_\star$ and $L_\star/M_e$ vary with t. For each time t, each specified value of $L_\star$ and $L_\star/M_e$ corresponds to a particular value of τ_{IR}, given by equation (14) in the optically thick approximation, or by equation (21) in the optically thin approximation. These value of τ_{IR} determine T_{bol} in equation (24a) (thick) or equation (24b) (thin). At present there are two well-known models of $L_\star(t)$, due to infall luminosity for protostars (e.g., Adams & Shu 1985, 1986) and to quasi-static contraction for pre–main-sequence stars (e.g., D'Antona & Mazzitelli 1994), but there is no well-established model of envelope dissipation which would predict $M_e(t)$. Therefore, we present a simple formulation which describes the dissipation of the envelope, matches available estimates of mass infall rates, and makes a smooth transition from infall to contraction luminosity.

3.1. Infall Evolution

The standard model of inside-out collapse of a singular isothermal sphere (Shu 1977) has a mass infall rate $dM/dt \approx \sigma_v^3/G$, independent of time, where σ_v is the velocity dispersion of the molecule of mean mass and G is the gravitational constant. This model by itself gives no way for the infall to stop, since the infall rate is constant and the isothermal sphere is infinitely extended. Estimates of dM/dt derived from observations decrease from $\sim 2 \times 10^{-6} M_\odot$ yr^{-1} at age ~ 0.3 Myr for low-mass protostars embedded in thick circumstellar envelopes (e.g., Adams & Shu 1986) to $\sim 10^{-8} M_\odot$ yr^{-1} at age 1–3 Myr for the more active optically visible T Tauri stars (Hartmann et al. 1997b). Evidently dM/dt decreases with time because infall of some circumstellar gas is accompanied by dispersal of the rest.

The leading candidate for this dispersal of circumstellar gas is the molecular outflow seen in a very high fraction of the most embedded YSOs (Bontemps et al. 1996; Terebey, Vogel, & Myers 1992; Bally & Lada 1983). Models of the jets and/or winds which drive such outflows link the driving energy to the gravitational energy associated with the infall (e.g., Königl & Ruden 1993; Shu et al. 1994). Thus it is reasonable to suppose that the timescales associated with the infall $t_\star$, and with the envelope dispersal, t_e, are similar, although not necessarily identical.

We model the mass infall rate to match the isothermal sphere infall solution at early times, but to decline at later times. We specify the envelope dissipation with a similar timescale. For simplicity we adopt exponential expressions for the dependence of the stellar envelope mass on time. These exponential expressions are highly idealized, but we believe they are each more realistic than the assumption of constant rates of stellar mass increase, or of envelope decrease. Isothermal sphere models with decreasing mass infall rate have been presented by Foster & Chevalier (1993). Thus we take

$$M_\star = M_{\star\infty}[1 - \exp(-t/t_\star)] \,, \tag{25}$$

where $M_{\star\infty}$ is the main-sequence mass of the star, and the infall timescale is

$$t_\star = M_{\star\infty} G/\sigma_v^3 \,. \tag{26}$$

The corresponding mass infall rate is

$$dM_\star/dt = (\sigma_v^3/G) \exp(-t/t_\star) \tag{27}$$

For early times, $t \ll t_\star$, equations (25)–(27) reduce to $M_\star = \sigma_v^3 t G^{-1}$ and $dM_\star/dt = \sigma_v^3 G^{-1}$ as the infall of an isothermal sphere (for simplicity we omit the coefficient 0.975 since its departure from unity is negligible compared to the uncertainties in the present model). For late times, $t \gg t_\star$, $M_\star$ approaches the main-sequence mass $M_{\star\infty}$ with $dM_\star/dt = (\sigma_v^3/G) \exp(-t/t_\star)$ approaching zero. For $M_{\star\infty} = 0.5 M_\odot$, and $\sigma_v = 0.19$ km s^{-1} as for gas at 10 K, this expression gives $dM_\star/dt = 7 \times 10^{-9}$ $M_\odot$ yr^{-1} at $t = 1$ Myr, in reasonable agreement with recent estimates for T Tauri stars (Hartmann et al. 1997b).

Similarly, the envelope mass evolves according to

$$M_e = M_{e0} \exp(-t/t_e) \,, \tag{28}$$

$$dM_e/dt = -(M_{e0}/t_e) \exp(-t/t_e) \,, \tag{29}$$

where M_{e0} is the envelope initial mass and where t_e is the envelope dissipation timescale. In relating equations (25)–(29) for infall and envelope dissipation there are two dimensionless parameters: the envelope "star formation efficiency" $\epsilon \equiv M_{\star\infty}/M_{e0}$ and the ratio of infall and dissipation timescales $\gamma \equiv t_\star/t_e$.

We have also investigated a simpler version of equations (25)–(29) where the timescales $t_\star$ and t_e are equal, whence the infall and dissipation rates maintain the constant ratio ϵ. This version is essentially the same as proposed by Bontemps et al. (1996) to account for the observed decrease of CO mass outflow rates with YSO age. Here we allow $t_\star$ and t_e to differ because we find that $t_\star$ needs to exceed t_e by a factor of a few, to account for both the L_{bol} and T_{bol} of most T Tauri stars, as discussed in § 4.

The gradual variation of $M_\star$ and M_e with time discussed here is an oversimplification of a more complex situation, which probably includes repeating events of short duration, seen in FU Ori objects and in the ejections in Herbig-Haro flows.

3.2. Infall Luminosity

The luminosity of the exponential infall reaches a peak significantly lower than that of a suddenly terminated SIS infall, but it lasts for a substantially longer time. To illustrate, we evaluate

$$L_{\rm in} = (\eta GM_\star \, dM_\star/dt)/r_\star , \tag{30}$$

where $r_\star$ is the stellar radius. In this simplified treatment we assume that the rate of mass increase from the envelope onto the disk equals that from the disk onto the star, and that the star is perfectly efficient in dissipating its energy of differential rotation, so that $\eta = 1$ (cf. the Appendix; Adams & Shu 1986). We refer to the resulting luminosity as "infall luminosity," denoting dynamical infall onto the star-disk system, as distinguished from the luminosity due to quasi-static stellar contraction.

From equations (25)–(27) and (30), the peak luminosity has the value

$$L_{\rm in, max} = \frac{M_{\star\infty} \sigma_v^3}{4 r_\star} = 4.12 \left(\frac{M_{\star\infty}}{M_\odot} \right) \left(\frac{T}{10 \text{ K}} \right)^{3/2} L_\odot , \tag{31}$$

assuming $r_\star = 3 \, R_\odot$, for an accreting protostar with normal deuterium abundance (Stahler 1988). $L_{\rm in, max}$ is less than in suddenly terminated infall by a factor of 4. This peak luminosity for gradually terminated infall occurs when the star has acquired half its final mass, at a time earlier by a factor ln 2 than the peak luminosity for suddenly terminated infall:

$$t_{L{\rm max}} = (\ln 2) t_\star = \frac{(\ln 2) GM_{\star\infty}}{\sigma_v^3} = 0.43 \left(\frac{M_{\star\infty}}{M_\odot} \right) \left(\frac{T}{10 \text{ K}} \right)^{-3/2} \text{Myr} . \tag{32}$$

We note that the relatively low values of luminosity, compared to those in the suddenly terminated SIS infall model, coincide more closely with the relatively low luminosities of a few $L_\odot$ observed in Taurus-Auriga (Kenyon et al. 1990; Kenyon & Hartmann 1995).

These luminosity relations are shown in Figure 3, which plots the variation of $M_\star$ and $L_{\rm in}$ with time for the model of exponential infall described in § 3.1 above, and for the standard model of a collapsing singular isothermal sphere (Shu 1977 with sudden termination, for a star of 0.5 $M_\odot$ forming in a core of temperature 10 K.

Figure 3 shows that for the adopted parameters the exponential infall reaches a peak luminosity of 2.1 $L_\odot$, smaller by a factor of 4 than that of the SIS infall with sudden termination; that it reaches this peak at 0.2 Myr, sooner by a factor of 1.4, and that it stays within a factor of 2 of its peak for 0.55 Myr, longer by a factor of 3.5. These differences arise because the exponential infall terminates more gradually than the suddenly terminated SIS infall.

3.3. Consistency of Luminosities, Times, and Temperatures

To specify the total stellar luminosity as a function of time it is necessary to combine the luminosities due to infall $L_{\rm in}$, from equation (30), and contraction $L_{\rm con}$, from DM, so that their timescales are consistent and their luminosities vary continuously.

DM provide values of $L_{\rm con}$ for times $t_{\rm con} = 0.07$–1000 Myr since the onset of contraction from infinite radius. The infall luminosity in equation (30) specifies $L_{\rm in}$ for a continuous range of times t since the onset of infall. The difference between the two zeros of time is known only approximately and is of order the free-fall time, a few $\times$ 0.1 Myr. We adopt 0.1 Myr, consistent with the estimate of Chen et al. (1995) and the discussion of Stahler (1983, 1988).

To obtain $L_{\rm con}(t)$ we take $t = t_{\rm con} + 0.1$ Myr, as discussed above, for the discrete values of $t_{\rm con}$ given by DM, and for stellar masses $M_\star(t) \geq 0.2 \, M_\odot$, calculated from equation (25). Thus, $L_{\rm con}$ first increases as the star continues to gain mass from infall and then decreases as the star approaches its final mass and contracts. The peak value of $\log L_{\rm con}$ is generally greater than the peak value of $\log L_{\rm in}$ by 0.1–0.2. We interpolate among stellar mass entries in DM Tables 1 and 5, using linear interpolation in the $\log t_{\rm con}$–$\log M_\star$ plane. The resulting values of $\log L_\star = \log [L_{\rm con}(t) + L_{\rm in}(t)]$ are plotted against $\log L_\star/M_e$. Usually there is a small abrupt increase, by ~ 0.1 in $\log L_\star$, due to the lack of DM values of $\log L_{\rm con}$ for times $t_{\rm con} < 0.07$ Myr. Consequently, we fit a smooth curve through the values of $\log L_\star$ versus $\log L_\star/M_e$, as illustrated in Figure 4. We use these smooth curves to obtain plots of $\log L_\star$ versus $\log T_{\rm bol}$.

In combining infall and contraction luminosities we make the basic assumption that the total luminosity is the simple sum of the two luminosities determined separately. This assumption is a great oversimplification of a more complicated problem, the transition between the protostellar and pre–main-sequence phases of evolution. Detailed consideration of this problem is an important task (Mercer-Smith, Cameron, & Epstein 1984; Hartmann, Cassen, & Kenyon 1997a), but is beyond the scope of this paper. As a practical matter, however, the portion of the BLT diagram where the two luminosities are comparable is very small; for most evolutionary times either one luminosity or the other clearly dominates.

The uniform temperature T of the isothermal sphere assumed in § 2.8.1 as the basis of the infalling system is formally inconsistent with the centrally elevated temperature structure, either $T \sim r^{-1/2}$ (optically thick) or $T \sim r^{-2/5}$ (optically thin), assumed for the envelope once a star has formed. The central heating makes only a small difference to the infall process, compared to an isothermal infall, because most of the mass comes from the outer parts of the envelope where the temperature is nearly isothermal. To reconcile the two temperatures we assume that the isothermal temperature T in equations (25)–(30) equals the envelope outer boundary temperature T_2 in equations (14) and (21).

4. BOLOMETRIC LUMINOSITY AND TEMPERATURE PLOTS

It is now possible to predict the evolution of $T_{\rm bol}$ and $L_{\rm bol}$ as an envelope of initial mass M_{e0} and temperature T dissipates
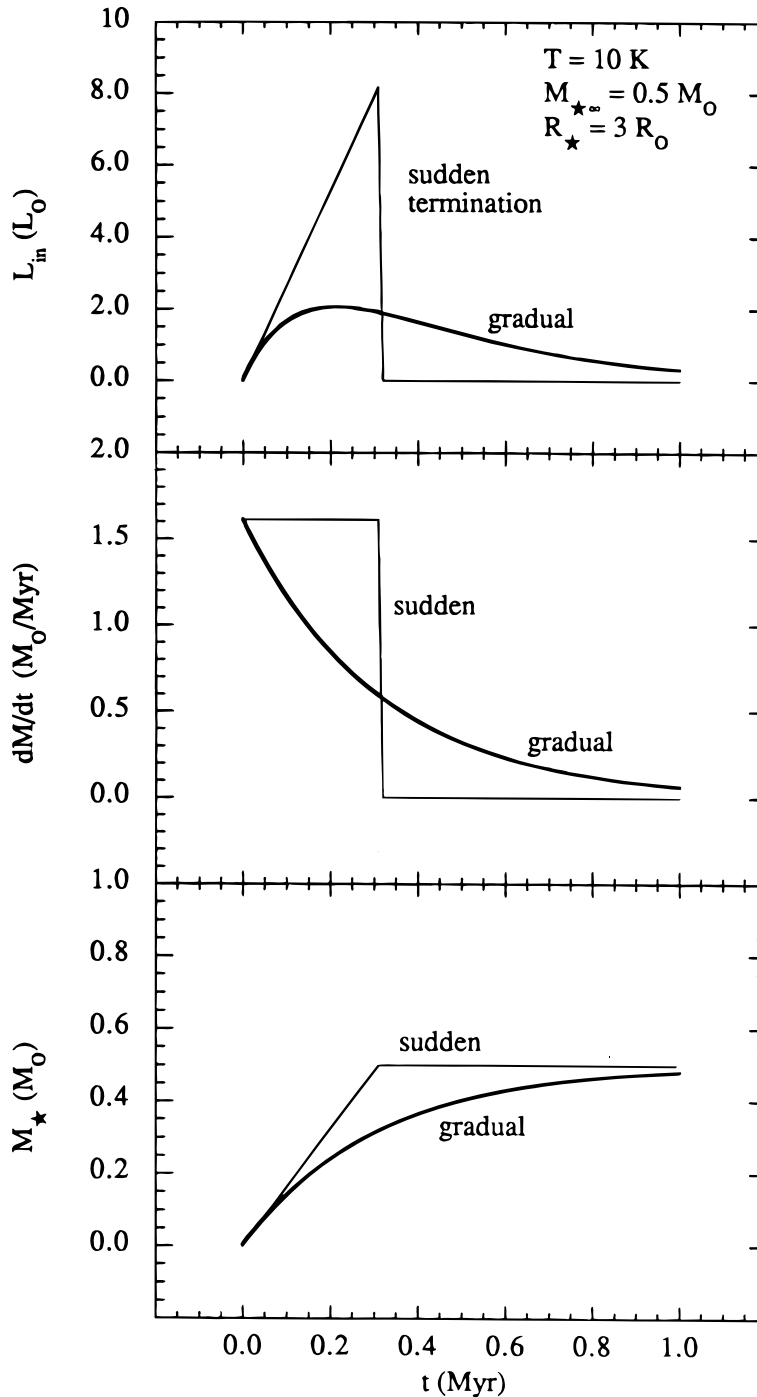
FIG. 3.—Time evolution of two versions of gravitational infall for a 10 K singular isothermal sphere forming a 0.5 $M_\odot$ star. Light lines indicate infall which is terminated "suddenly," while heavy lines indicate infall which is terminated "gradually" according to the exponential law in the text. The upper, middle, and lower panels show, respectively, the infall luminosity, the mass infall rate, and the accumulated stellar mass vs. the time since the start of infall. The gradual and sudden cases have the same initial properties, but the gradual case reaches a peak luminosity smaller by a factor 4 than does the sudden case, and because it provides a smoother transition between protostellar and pre–main-sequence evolution.

on a timescale t_e and forms a star of mass $M_\star$. Table 1 summarizes the fixed parameter values adopted in the development of § 2. Table 1 lists all the fixed parameters needed in addition to the four adjustable parameters, to specify the model tracks of $L_{bol}(t)$ versus $T_{bol}(t)$. In this section we present parameter studies of evolutionary tracks in the log L_{bol}–log T_{bol} plane (BLT diagram), and a set of tracks based on these studies which appears to correspond most closely to observed properties of YSOs. We vary the essential parameters T, $M_\star$, M_{e0}, and t_e in equations (27)–(32), or equivalently, T, $M_\star$, ϵ, and γ.

4.1. Parameter Variation

In the following sections we consider tracks in the BLT diagram for stellar masses $M_{\star\infty}$ = 0.3, 0.5, and 0.7 $M_\odot$; outer envelope temperature T = 8, 10, and 12 K; initial envelope mass M_{e0} = 1, 3, and 10 $M_\odot$; and ratio of stellar and dissipation timescales γ = 2, 3 and 5. For each BLT diagram we plot for reference the zero-age main sequence, as given by D'Antona &

TABLE 1

ADOPTED FIXED PARAMETERS

Parameter	Equation of First Use	Adopted Value	Comment
T_0	1	1500 K	Dust destruction temperature
A	12	1.59×10^{-13} cm^2 g^{-1} Hz^{-1}	Coefficient of emissivity power law
κ_{IR}	12	4 cm^2 g^{-1}	Emissivity at 12 μm
κ_E	16	6 cm^2 g^{-1}	Energy-weighted emissivity
τ_a	22	1	Sets variation of f from 0 to 1/4
τ_b	22	3	Sets variation of f from 1/4 to 1
τ_0	...	0.05	Value of τ_{IR} dividing optically thick and thin approximations
$r_\star$	32	2.1×10^{11} cm	Protostellar radius

Mazzitelli (1994), and lines indicating the values of T_{bol} which divide the spectral classes 0, I, II, and III (Lada & Wilking 1984; André et al. 1993; Chen et al. 1995). Each track is marked where the time t since the start of infall satisfies $\log(t\,\mathrm{Myr}^{-1}) = -1.5, -1.0, -0.5$, and 0.

Figure 5 shows BLT tracks for stellar mass $M_{\star\infty} = 0.3, 0.5$, and $0.7\,M_\odot$, with fixed values $\gamma = 3$, $T = 10$ K, and $M_{e0} = 3\,M_\odot$. With increasing stellar mass the peak luminosity increases, due mainly to the strong dependence of the contraction luminosity on mass. However, the starting luminosity depends on the envelope temperature, not the stellar mass, so the low-T_{bol} portions of the tracks are nearly identical. The change in slope of each track near $\log T_{bol} = 3.5$ marks the transition between the optically thick and thin approximations.
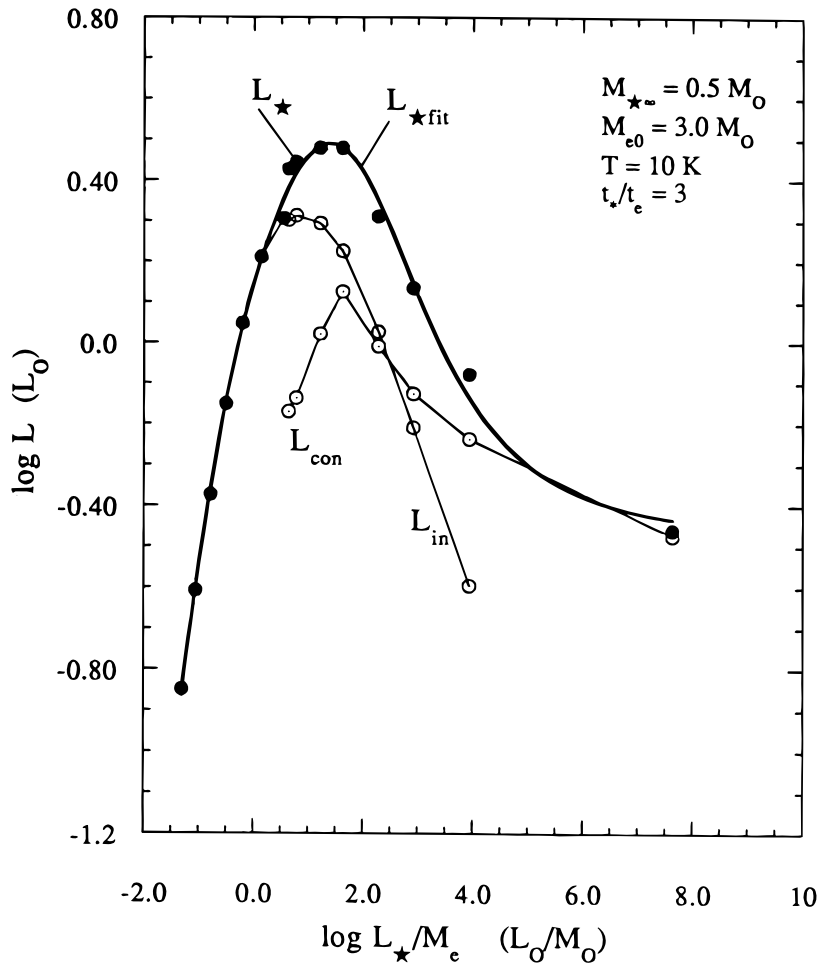

FIG. 4.—Relation of infall luminosity L_{in} (open circles), contraction luminosity L_{con} (open circles with dots), and stellar luminosity $L_\star \equiv L_{in} + L_{con}$ (filled circles) to the ratio of stellar luminosity and envelope mass $L_\star/M_e$, for standard parameter values. The solid curve shows $L_{\star fit}$, the best-fit curve to the values of $L_\star$, with functional form

$$y = a + b\left\{\frac{1 - \exp[-c(x - d)]}{1 + e|x|^{3.5}}\right\}$$

where $x = \log L_\star/M_e$, $y = \log L_{\star fit}$, and a, b, c, d, and e are parameters determined by a nonlinear least-squares fitting program.
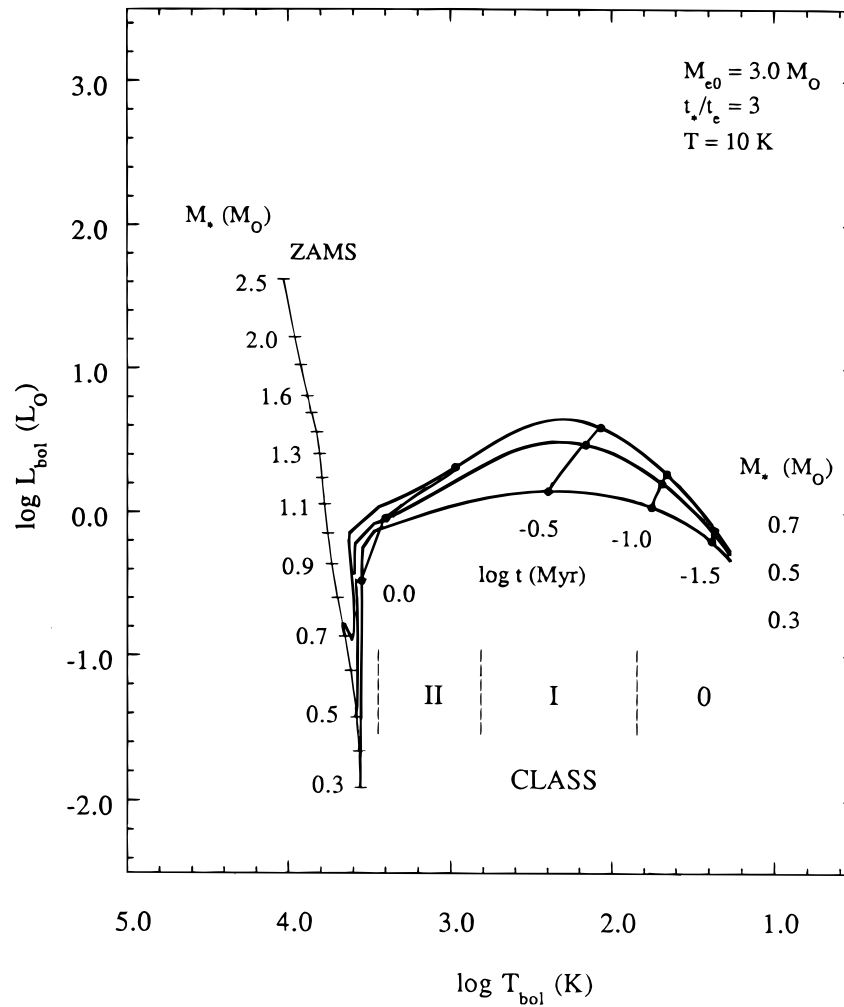
Fig. 5.—BLT diagram tracks for final stellar mass 0.3, 0.5, and 0.7 $M_\odot$, with initial envelope mass $M_{e0} = 3.0\ M_\odot$, ratio of infall and envelope dissipation timescales $t_\star/t_e = 3$, and outer envelope temperature $T = 10$ K. Filled circles indicate time t (Myr) since the star of infall, at $\log t = -1.5, -1.0, -0.5$, and 0.0. Vertical lines indicate boundaries between spectral classes of Lada & Wilking (1984) and André et al. (1993), according to Chen et al. (1995). The light line with ticks indicates the zero-age main sequence given by D'Antona & Mazzitelli (1994).

Figure 6 shows the effect of varying the ratio γ of stellar and dissipation timescales from 2 to 5, while $M_{\star\infty} = 0.5\ M_\odot$, $M_{e0} = 3\ M_\odot$, and $T = 10$ K. During the infall phase there is little difference among tracks, but in the contraction phase the change of shape is dramatic, with increasing γ giving more rapid envelope dissipation. For $\gamma = 5$, $T_{\rm bol}$ increases to ~ 3000 K before $L_{\rm bol}$ has time to descend the Hayashi convective track. In this case the evolution after ~ 1 Myr is essentially the same in the BLT diagram as on the H-R diagram, with $T_{\rm bol} \approx T_\star$. In contrast, for $\gamma = 2$, the envelope is slow to dissipate, and the Hayashi track starts at about $T_{\rm bol} \approx 1000$ K.

Figure 7 shows the effect of changing the initial envelope mass from $M_{e0} = 1$ to 3 to 10 $M_\odot$, while $M_{\star\infty} = 0.5\ M_\odot$, $\gamma = 3$, and $T = 10$ K. Increasing envelope mass increases the optical depth, so the tracks reach their peak luminosity at progressively lower values of $T_{\rm bol}$. The track for $M_{e0} = 10\ M_\odot$ passes through $(T_{\rm bol}, L_{\rm bol}) = (30$ K, 2 $L_\odot)$, values similar to those of B335 (Chandler et al. 1990).

Figure 8 shows changes in outer envelope temperature $T = 8$, 10, and 12 K, with fixed $M_{\star\infty} = 0.5\ M_\odot$, $M_{e0} = 3\ M_\odot$, and $\gamma = 3$. The tracks have similar shape, and are displaced upward with increasing T. This behavior is easily understood for the optically thick approximation, where the luminosity is dominated by infall luminosity. Then equations (12)–(14) and equation (24a) imply $L_{\rm bol} \sim M_e(t) T_{\rm bol}^2 T^3$. Thus for fixed time and $T_{\rm bol}$, $L_{\rm bol}$ increases as T^3, in accord with the values shown in Figure 8.

Figure 9 shows tracks for a combination of outer envelope temperature T and final stellar mass $M_{\star\infty}$ chosen to correspond to core initial conditions. YSOs in warmer dense cores tend to have greater mass, even for low-mass YSOs where the central heating by the embedded star is probably too small to account for the observed increase in temperature (Myers, Ladd, & Fuller 1991, hereafter MLF). Instead, MLF suggest that increased temperature and turbulence are in part initial conditions and not solely the consequences of more massive star formation. The idea that increased temperature and turbulence lead to higher mass stars has been developed into a theory of the initial mass function (Adams & Fatuzzo 1996). Accordingly, Figure 9 associates $T = 8$ K with $M_{\star\infty} = 0.3\ M_\odot$, $T = 10$ K with $M_{\star\infty} = 0.5\ M_\odot$, and $T = 12$ K with $M_{\star\infty} = 0.7\ M_\odot$.

The tracks in Figure 9 have similar shape but are displaced from each other by 0.2–0.4 in $\log L_\star$. This behavior differs from the tracks for fixed temperature but varying mass (Fig. 5), which are well-separated at intermediate values of $T_{\rm bol}$, but which converge at low and high values of $T_{\rm bol}$. This behavior also differs from the tracks for fixed mass but varying temperature (Fig.
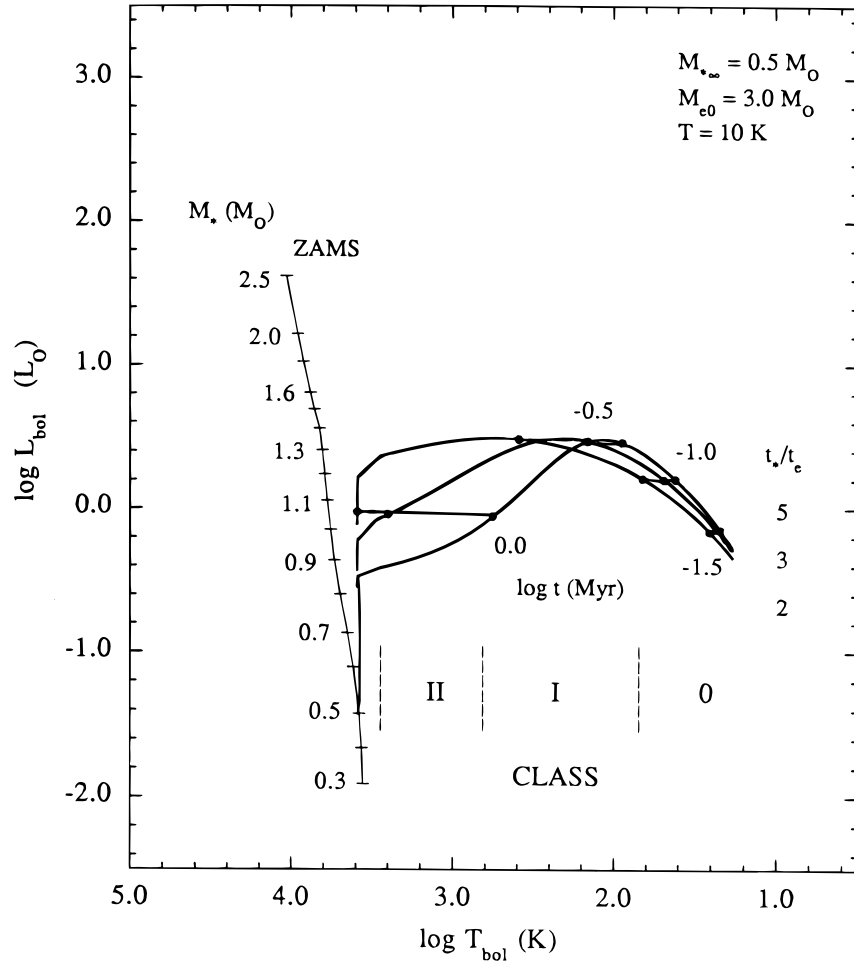
FIG. 6.—BLT diagram tracks for ratio of infall and envelope dissipation timescales $t_{\star}/t_e = 2$, 3, and 5, with final stellar mass $M_{\star\infty} = 0.5\ M_{\odot}$, initial envelope mass $M_{e0} = 3.0\ M_{\odot}$, and outer envelope temperature $T = 10$ K. Other symbols are as in Fig. 5.

8), which are separated by only 0.1–0.2 in log $L_{\star}$. Evidently the combination of increasing $M_{\star\infty}$ with increasing T gives tracks with greater and more uniform separation than with either fixed $M_{\star\infty}$ or fixed T. We adopt this set of T and $M_{\star\infty}$ because it is justified by the core-star association demonstrated by MLF, and because the resulting separation of track luminosities is greater, as is needed to match the spread in observed luminosities.

For each adopted track in Figure 9, an open circle (labeled " $L_{\text{in}} = L_{\text{con}}$ " on the uppermost track) marks the point in our model where the infall and contraction luminosities are equal. This point can be considered to separate "protostellar" and "pre–main-sequence" portions of YSO evolution; it occurs near $T_{\text{bol}} = 2800$ K, the transition from class II to III, at an age of about 1 Myr.

There is little observational basis a priori to guide particular choices of the efficiency ϵ or the ratio of timescales γ. The efficiency depends on the initial envelope mass M_{e0}, as shown in Figure 7. The ratio of timescales has a more significant effect on the shape and location of the tracks, as shown in Figure 6. We estimate the likely range of γ to be 2–5 as in Figure 6 because then the positions of well-studied T Tauri stars in Lupus, having careful estimates of mass 0.3–0.7 $M_{\odot}$ (Hughes et al. 1994; Chen et al. 1997) fit best between the tracks. A more complete theory of protostellar infall, combined with disk accretion, is needed to address this question (see Yorke, Bodenheimer, & Laughlin 1995; Hartmann et al. 1997).

4.2. Features of the BLT Diagram

The most prominent feature of the BLT diagram in Figure 9 is the peak luminosity at $T_{\text{bol}} = 200$–600 K, near the maximum L_{in}. In all cases L_{bol} increases due to infall and then decreases due to contraction, as T_{bol} increases. The peak total luminosity is generally greater by a factor ~ 1.5 than the peak infall luminosity, given by equation (31). In the optically thick approximation, which is most likely to apply at this early time, this luminosity occurs at a T_{bol} given by equations (12), (14), (28), and (31) as

$$T_{\text{bol}}(L_{\text{max}}) = \frac{\Gamma(9/2)\zeta(9/2)}{\Gamma(5)\zeta(5)} \left(\frac{hk^{1/2}}{6A\sigma r_{\star}\ m^{3/2}T_2^{3/2}} \right)^{1/2} \left(\frac{M_{\star\infty}}{M_{e0}} \right)^{1/2} \exp\left[\frac{t_{\star}\ln 2}{2t_e} \right], \tag{33a}$$

$$T_{\text{bol}}(L_{\text{max}}) = 83 \left(\frac{T_2}{10\ \text{K}} \right)^{-3/4} \epsilon^{1/2} \exp\left[0.35\gamma \right]\ \text{K}, \tag{33b}$$
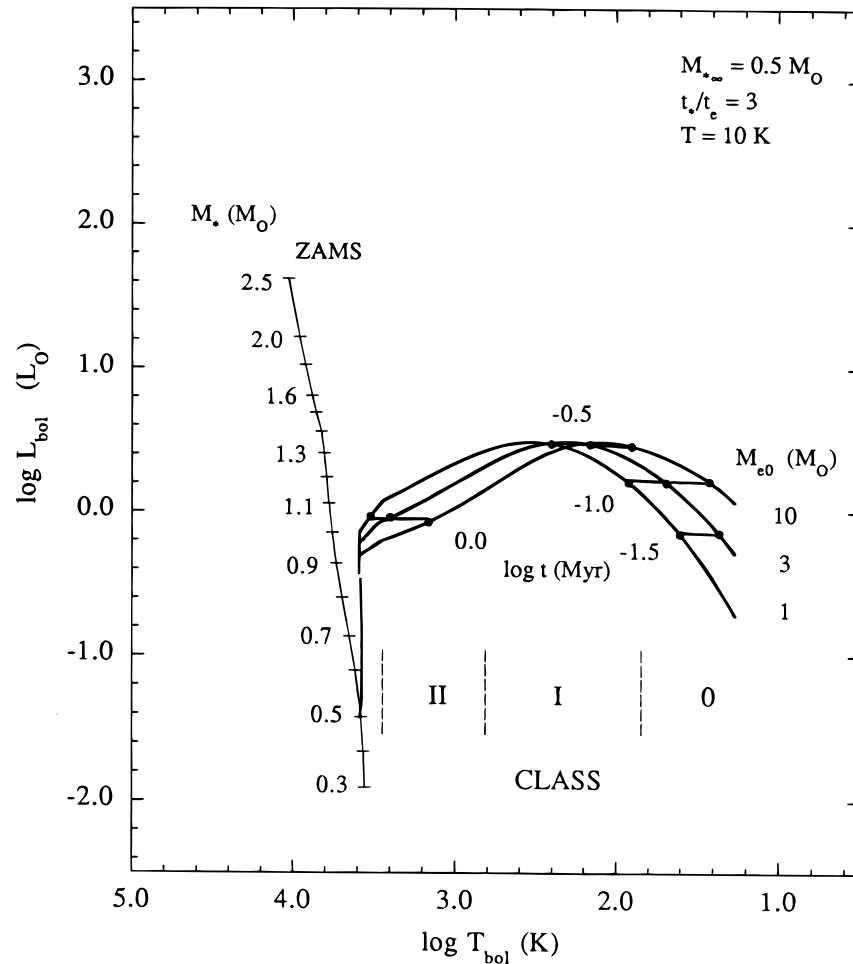
Fig. 7.—BLT diagram tracks for initial envelope mass $M_{e0} = 1$, 3, and 10 $M_\odot$, with final stellar mass $M_{\star\infty} = 0.5$ $M_\odot$, ratio of infall and envelope dissipation timescales $t_\star/t_e = 3$, and outer envelope temperature 10 K. Other symbols are as in Fig. 5.

where we use in equation (33b) the efficiency ϵ and timescale ratio γ defined in § 3.1. Thus envelopes with temperature $T_2 = 10$ K, forming stars of mass 0.3–0.7 $M_\odot$, with efficiency 0.3–0.5, and with ratio of infall and dispersal timescales equal to 3–5, should reach peak infall luminosities of 1–3 $L_\odot$ at 0.1–0.3 Myr, with $T_{bol} = 130$–340 K. These numbers correspond closely to "class I" YSOs (e.g., Chen et al. 1995).

The model evolution of a YSO can now be described with reference to the tracks in Figure 9. For example, a core with initial mass 3 $M_\odot$ and temperature 10 K, forming a star of main-sequence mass 0.5 $M_\odot$ with dissipation timescale 0.1 Myr, spends most of its first 0.1 Myr as a class 0 YSO, after which it has $T_{bol} = 70$ K and $L_{bol} = 2.2$ $L_\odot$ due to infall. For the next 0.4 Myr its T_{bol} is that of a class I YSO, and it reaches its peak luminosity of 3.8 $L_\odot$ as its infall luminosity begins to decline and its contraction luminosity is at its maximum. As it starts its class II phase it has $T_{bol} = 650$ K, $L_{bol} = 2.6$ $L_\odot$, due more to infall than to contraction, and its mass is 0.4 $M_\odot$, nearly all of its main-sequence mass. For the next 1.5 Myr its T_{bol} is that of a class II source, a T Tauri star with a disk and an envelope. During this phase the star contracts, the envelope dissipates, and the circumstellar extinction decreases. As it starts its class III phase its luminosity starts to be dominated by contraction, rather than infall; it is visible only in the optical and near-infrared, with $T_{bol} = 2800$ K and $L_{bol} = 0.7$ $L_\odot$. In its class III phase it dissipates its envelope and optically thick disk, and joins the convective pre–main-sequence tracks as calculated by DM, evolving toward the zero-age main sequence.

4.3. Comparision with Observations

The BLT plots of YSOs in Taurus (ML), Ophiuchus (Chen et al. 1995), and Corona Australis, Lupus, and Chamaeleon (Chen et al. 1997) span values of T_{bol} from ~ 50 to ~ 5000 K, and of L_{bol} from ~ 0.1 to ~ 100 $L_\odot$. The tracks presented in Figure 9 span this range of T_{bol} and thus account for the colors of far more YSOs than can be represented on the H-R diagram. Similarly, the tracks in Figure 9, and the analogous tracks for higher masses, span the range of luminosities observed in nearby star-forming complexes.

More detailed comparison with observed YSOs must take into account the relative timescales of the different spectral classes and the numbers of YSOs in a complex. For example, consider the timescales discussed in § 3.2 for cores forming stars of mass 0.5 $M_\odot$, and assume a constant birthrate starting 5 Myr ago. Then one would expect that in Figure 9 a complex of 100 YSOs along the 0.5 $M_\odot$ track would have approximately 60 YSOs in class III, 30 in class II, 8 in class I, and 2 in class 0. Taking a range of stellar masses into account, this pattern would extend upward for more massive stars and downward for less massive stars. For a stellar mass range from 0.3 to 0.7 $M_\odot$, one would expect to see points filling the left half of the
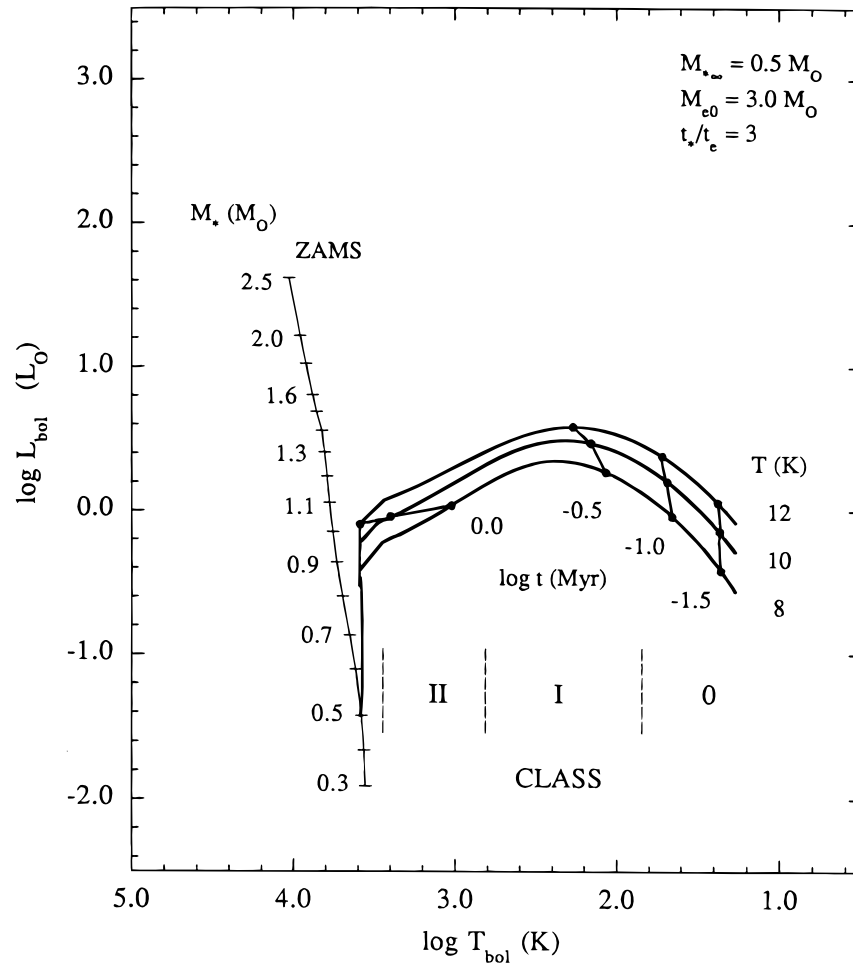
FIG. 8.—BLT diagram tracks for outer envelope temperature 8, 10, and 12 K, with final stellar mass $M_{\star\infty} = 0.5\ M_\odot$, initial envelope mass $M_{e0} = 3\ M_\odot$, and ratio of infall and envelope dissipation timescales $t_\star/t_e = 3$. Other symbols are as in Fig. 5.

arch-shaped region bounded by the tracks in Figure 9, with luminosity increasing and density of points decreasing from class III to II to I. Small numbers would generally limit the chance to see a statistically significant decrease from the luminosities of class I to class 0. Thus one would expect the BLT diagram of a well-developed low-mass star-forming complex with a constant birthrate to have a high density of sources with $\log L_{bol} = -1$ to 0, and $\log T_{bol} > 3$; and sources with density lower by a factor of order 10, having $\log L_{bol} = 0$–1, and $\log T_{bol} = 2$–3.

Among BLT diagrams of the five nearest star-forming complexes (Taurus, Ophiuchus, Corona Australis, Chamaeleon, and Lupus (ML; Chen et al. 1995; Chen et al. 1997), the half-arch pattern described above is most clearly seen for the largest possible sample with the greatest statistical significance. Figure 10 shows the "median BLT diagram" for all 362 YSOs in Lupus, Chamaeleon, Taurus, Ophiuchus, and Corona Australis having at least 6 spectral measurements, to provide accurate estimates of T_{bol}, and having $T_{bol} > 0.1\ L_\odot$, to minimize bias due to variations in sensitivity at different wavelengths (Chen et al. 1997). For each of 33 bins the vertical line at the median T_{bol} spans the central four deciles of L_{bol}, a range intermediate between two standard deviations and two quartiles. The median L_{bol} generally lies close to the center of the vertical line. As discussed by Chen et al. (1997), this median BLT diagram shows a distinct decrease in L_{bol} with increasing T_{bol}, from $\log L_{bol} \approx 0.5$ at $\log T_{bol} \approx 2.0$ to $\log L_{bol} \approx -0.3$ at $\log T_{bol} \approx 3.5$.

Figure 10 also shows a second feature for hotter stars, a distinct increase in L_{bol} with increasing T_{bol}, from $\log T_{bol} = 3.5$ to 3.8, running parallel to the main sequence and displaced to lower temperatures by a factor ~ 2. We interpret this feature as arising from older, more massive stars which have dissipated their envelopes but which still have substantial infrared excess due to their circumstellar disks.

We show in Figure 11 the relation of the observed median BLT diagram, in Figure 10, for the 24 bins spanning $\log T_{bol} = 2.0$ to 3.5, to the evolutionary tracks in Figure 9. This range of T_{bol} is chosen to exclude the hotter, and presumably more massive, stars in Figure 10, reducing the number of YSOs in the sample from 362 to 254. The observed medians lie between the lower and upper tracks corresponding to 0.3 and 0.7 $M_\odot$ in 21 of 24 cases, and the four-decile range of observed luminosities generally spans 0.5–1.5 times the range of $\log L_{bol}$ corresponding to 0.3–0.7 $M_\odot$. This close correspondence between observed and model BLT distributions supports the validity of the model described in §§ 2–3. It suggests that the typical YSO in the nearest star-forming complexes, including those which are optically invisible, has mass between 0.3 and 0.7 $M_\odot$, as expected from spectroscopic studies of optically visible stars alone (e.g., Kenyon & Hartmann 1995). It will be important to extend the observations of nearby "class 0" sources to more spectral points, so that their positions on the BLT diagram can be compared to those expected from Figure 11.
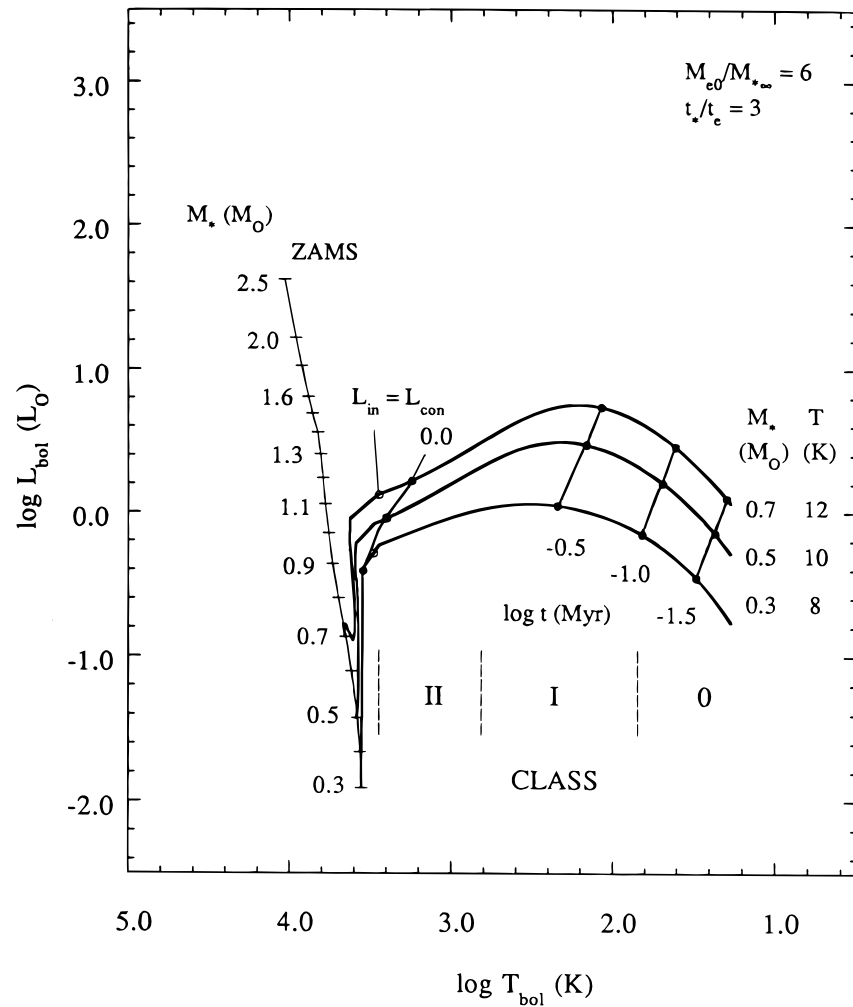
FIG. 9.—Adopted BLT diagram tracks for outer envelope temperature 8 K and final stellar mass 0.3 $M_\odot$; 10 K and 0.5 $M_\odot$; and 12 K and 0.7 $M_\odot$; with ratio of infall and envelope dissipation timescales $t_*/t_e = 3$ and with ratio of initial envelope mass and final stellar mass $M_{e0}/M_{*\infty} = 6$. The open circles marked $L_{in} = L_{con}$ indicate where infall and contraction make equal contributions to the total stellar luminosity. Other symbols are as in Fig. 5.

Among the five nearest star-forming complexes, the model predictions in Figure 9 are matched most nearly by the Ophiuchus complex. There the class I sources have typical $L_{bol} = 10\ L_\odot$, and are clearly more luminous than the class II sources, by a factor ~ 10, as noted earlier (Kenyon et al. 1990; Greene et al. 1994). This pattern is not fit perfectly since there is also a substantial number of relatively luminous class III sources, presumably belonging to an older, more massive population. Also, the core of the L1686 cloud in Ophiuchus has both high obscuration and high source density, making it difficult to detect low-luminosity sources. If the luminous class I sources in Ophiuchus have their peak luminosity due to contraction and accretion as in § 3.2, in an envelope with $T = 15$ K, their age since the start of infall is 0.3 Myr and their typical mass is 0.9 $M_\odot$. This mass is substantially greater than the $\sim 0.5\ M_\odot$ generally associated with young stars in Taurus (Kenyon & Hartmann 1995), Lupus (Hughes et al. 1994), and Chamaeleon (Hartigan 1993).

Among other nearby complexes, the half-arch pattern also appears in the BLT diagram for Chamaeleon, although less clearly than in Ophiuchus. In Chamaeleon, the median class I luminosity is $\sim 10\ L_\odot$ among six YSOs, while the median class II luminosity is $0.4\ L_\odot$ among 44 YSOs. Thus the class I sources in Chamaeleon also appear to have luminosity consistent with main-sequence mass of $\sim 1\ M_\odot$. However, dense core temperatures in Chamaeleon are probably closer to 10 K than 15 K (Vilas-Boas, Myers, & Fuller 1994), so the time for their YSOs to reach $10\ L_\odot$ would be closer to 0.6 Myr than the 0.3 Myr estimated above for a 15 K core, from equation (32). As with Ophiuchus, Chamaeleon also has a population of more luminous class III sources. In Lupus and Corona Australis, there are too few class I sources to make a statistically useful comparison.

In Taurus, the median class I luminosity exceeds the median class II luminosity by a factor of 2, but only when sources with poorly defined peaks are excluded (see Chen et al. 1995). When all Taurus sources are considered, there is no significant decrease in luminosity with increasing T_{bol}. Unlike Lupus and Corona Australis, Taurus has a significant number of well-studied YSOs of all spectral classes (Kenyon & Hartmann 1995). Thus the flat distribution of Taurus sources in the BLT diagram should be considered as a significant departure from the distributions in the Ophiuchus and Chamaeleon complexes, and from the model tracks shown in Figure 11.

To account for the preponderance of low-luminosity class I sources in Taurus, in the context of the model presented in this paper, we offer the following speculation. In Taurus, a significant number of very low-mass stars, with $M_{*\infty} = 0.1$–$0.3\ M_\odot$, may have started their infall phase a few times 0.1 Myr ago. These could have come from the same "generation" of cores, the denser, faster-evolving members of which produced more massive stars (0.3–0.7 $M_\odot$) earlier, and whose less dense, slower-
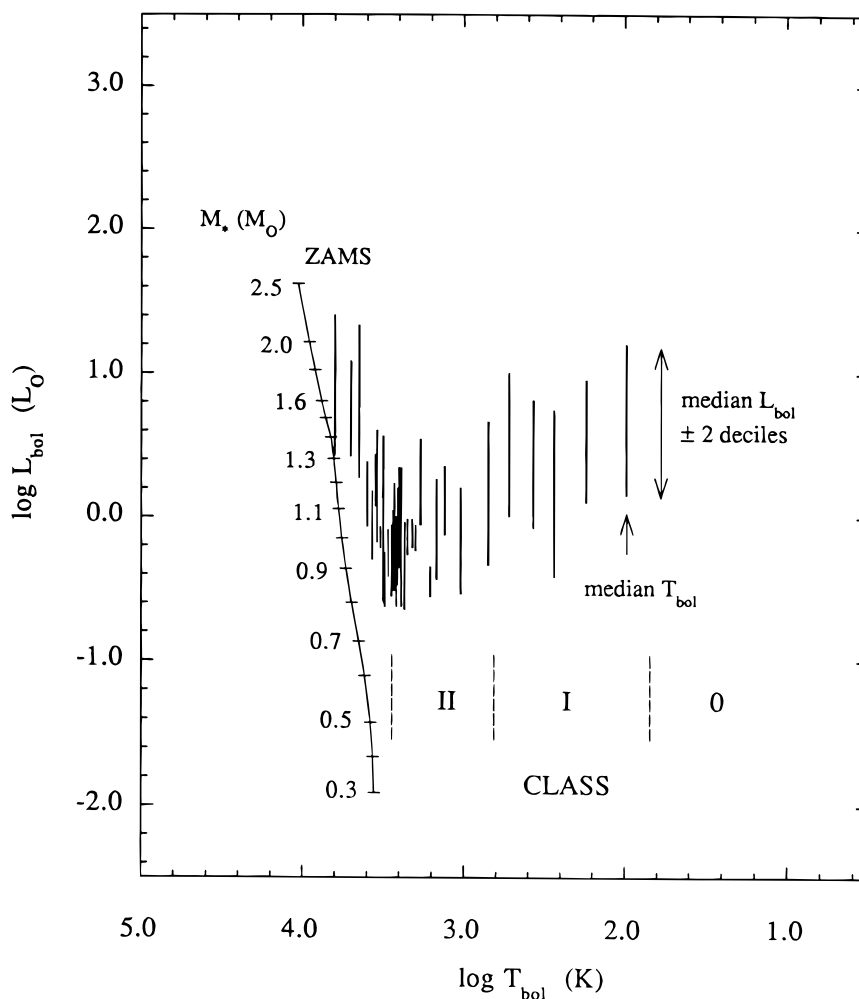
FIG. 10.—Observed BLT diagram for 362 young stellar objects in Chamaeleon, Corona Australis, Lupus, Ophiuchus, and Taurus (Chen et al. 1997). To minimize bias due to differing sensitivity at long and short wavelengths, only YSOs with $L_{bol} > 0.1\ L_\odot$ are included. To represent typical values and ranges, the data are ranked in T_{bol} and binned in groups of 11. Each vertical line is drawn at the median T_{bol} for its group, between endpoints which represent the third and seventh deciles of L_{bol}. Other symbols are as in Fig. 5.

evolving members produced less massive stars (0.1–0.3 $M_\odot$) later. If so, such YSOs would populate the BLT diagram in the range $2 < \log T_{bol} < 3$ and $-1 < \log L_{bol} < 0$, as observed. This behavior might also be expected for other complexes such as Lupus and Chamaeleon which tend to produce stars in "isolated" rather than "cluster" mode. However, these regions are not so well-studied in the near-infrared and submillimeter as is the Taurus complex. Thus there may not be as high a proportion of YSOs in the bottom center of the BLT diagram for Lupus and Chamaeleon as for Taurus, because of greater incompleteness. More sensitive observations in these three complexes should clarify this question.

4.4. An Evolutionary Sequence

It is useful to provide examples of YSOs which illustrate the trends shown by the medians in Figure 11. For this purpose we show in Figure 12 the BLT diagram for 14 well-studied YSOs of classes 0, I, II, and III, whose estimated ages span about 1 Myr. These sources are well-studied in the sense that their spectra generally have at least six photometric measurements, so that the estimates of T_{bol} and L_{bol} are reliable. The values of T_{bol} and L_{bol} are taken from Bachiller (1996), from Chen et al. (1995), Chen et al. (1997), and from Mardones et al. (1997). Each YSO is labeled with its most commonly known name, as given in its reference.

These 14 YSOs illustrate an evolutionary sequence not just in terms of model age, but also in terms of hallmarks of development: association with dense gas, molecular outflows, and optical line emission indicative of circumstellar material. The youngest sources, the class 0 sources VLA 1623, 03282, and L1527, are well-known sources with hallmarks of extreme youth: they are optically invisible, bright in the submillimeter, and drive well-collimated outflows. VLA 1623 and L1527 are also kinematic infall candidates (Mardones et al. 1997). According to our model they have ages <0.1 Myr. Of the class I sources L1551NE, 04365, 04016, CrAR1, IRS 63, and 04113, all are *IRAS* sources and most have known outflows (Wu, Huang, & He 1996). Their model ages range from 0.1 to 0.6 Myr. Of the class II sources 04299, FS Tau, and DoAr24, none has a known associated outflow, and two are classical T Tauri stars. These have model ages 0.6–1.0 Myr. Finally the class III sources LkCa5 and 043124 are weak-line T Tauri stars, with no associated dense gas, little infrared excess, and age >1 Myr according to both their position on the H-R diagram and to the present model.
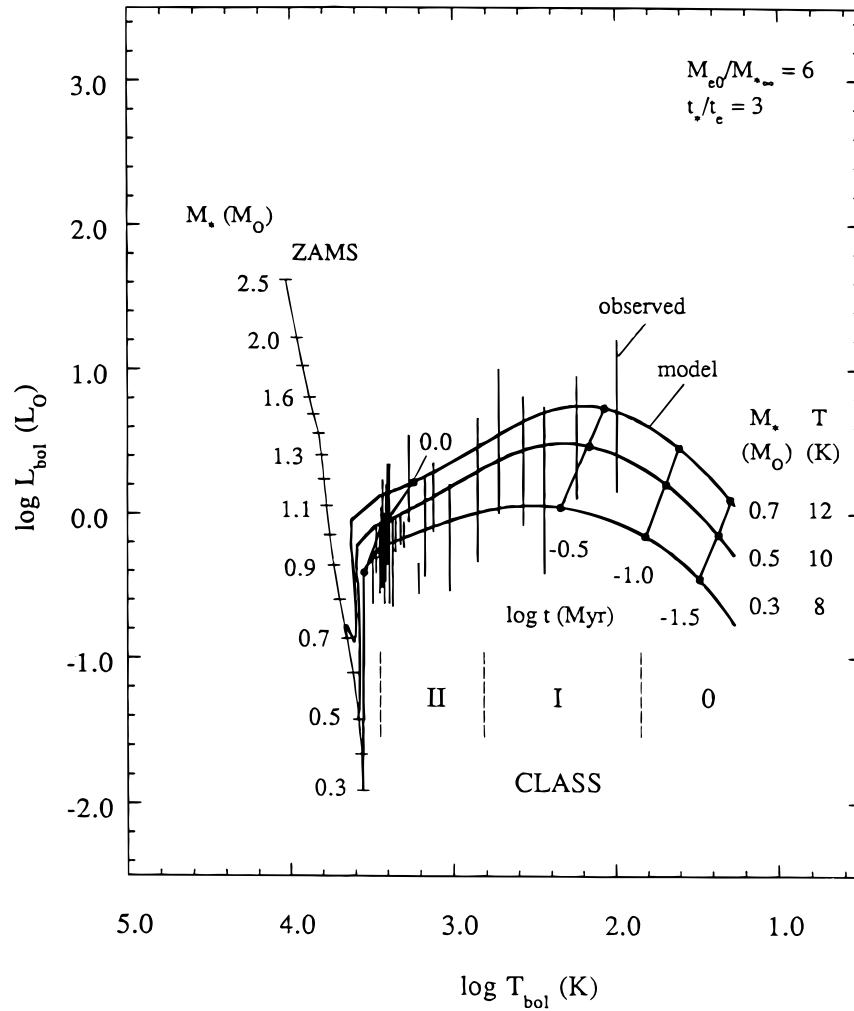
FIG. 11.—Relation of BLT diagrams observed (*vertical lines*), as in Fig. 10, and modeled (*curved lines*), as in Fig. 9. Other symbols are as in Fig. 5. The observations and models agree well, indicating that the model describes the main spectral properties of YSOs with mass 0.3–0.7 $M_\odot$ in nearby star-forming regions.

4.5. Departures from Spherical Symmetry

The foregoing models assume spherical symmetry of the circumstellar envelope and do not take into account observed departures from spherical symmetry, associated with jets and molecular outflows (e.g., Bontemps et al. 1996; Fukui et al. 1993). Also, the present models do not consider the polar flattening expected from models of rotating cores (Terebey et al. 1984) or magnetized cores (e.g., Mouschovias 1987). The orientation of an aspherical envelope with respect to the line of sight can affect the shape of the observed spectrum. If such changes are large enough, they can limit the utility of T_{bol}, or of the spectral classification of Lada & Wilking (1984) as indicators of evolutionary development (André 1995; Yorke et al. 1995, hereafter YBL).

To investigate the dependence of T_{bol} on orientation of an aspherical envelope, we consider a spherical envelope with the same properties as in § 2, except that a biconical volume within the envelope is now empty. This choice of geometry is motivated by observations of CO outflows, but it may also be considered an extreme case of the polar flattening expected for rotating or magnetized cores. The cavity has axial symmetry, and its symmetry axis and midplane pass through the center of the sphere. Since the system is symmetric and optically thick, we need only consider the forward hemisphere. The spherical part of the envelope has density $\rho \sim r^{-3/2}$ and temperature $T \sim r^{-1/2}$ for $r_1 \leq r \leq r_2$ as for the optically thick envelope in § 2.4.1. The emissivity is assumed to be $\kappa_0 = 5$ cm^2 g^{-1}, appropriate for class I sources with $T_{bol} = 100$–600 K, as discussed in the Appendix. The cavity has zero density for $r_1 \leq r \leq r_2$, inside an opening angle of θ, measured from the symmetry axis to the cavity wall. Except in the cavity, the system is assumed to be sufficiently optically thick to allow the "photospheric" approximation discussed in § 2.4.1.

We assume first that the system is viewed pole-on. In this case the viewing angle, ϕ, between the cavity axis and the line of sight is zero. Then the specific luminosity can be written, in a photospheric approximation similar to equation (8),

$$L_v = 8\pi \int_0^{r_2} b \, db B_v[T(r_{\tau=1})] \,, \tag{34}$$

where b is the offset perpendicular to the line of sight, $B_v(T)$ is the Planck function at temperature T and $T[r_{\tau=1}]$ is the temperature at the position $r_{\tau=1}$ defined by $r_{\tau=1}^2 = b^2 + z_{\tau=1}^2$, where $z_{\tau=1}$ is the position along the line of sight one optical
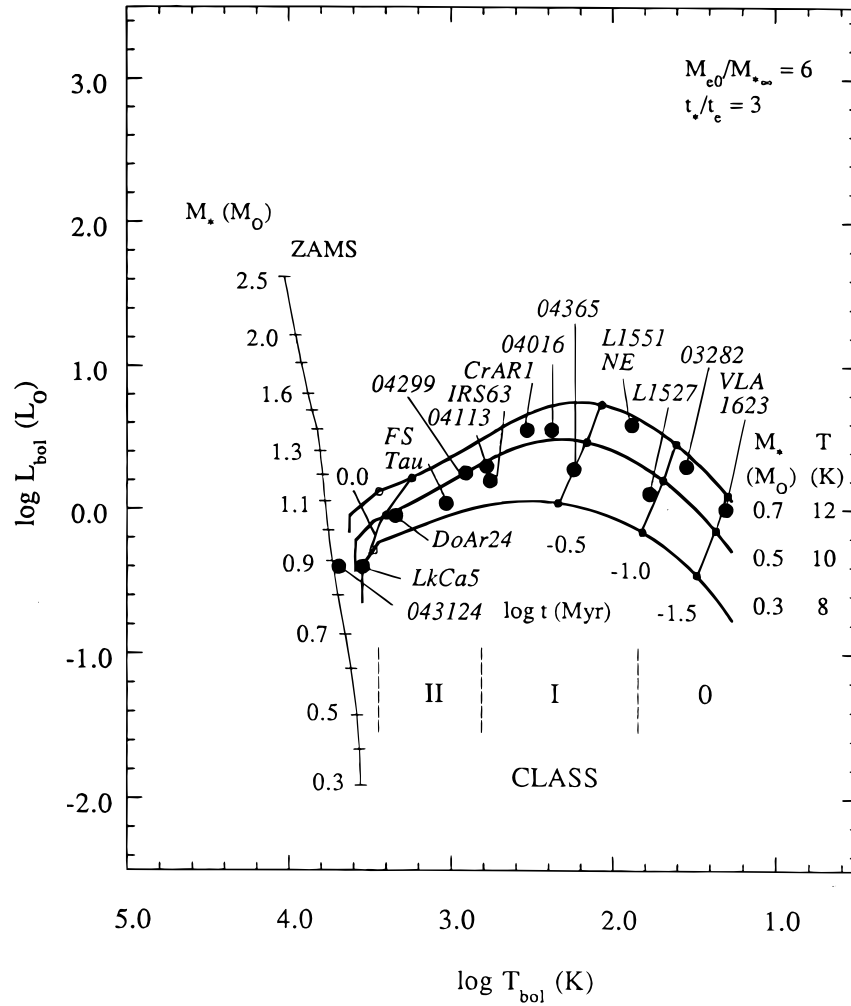
FIG. 12.—BLT diagram for 14 well-studied YSOs which follow the model tracks of Fig. 9. This "evolutionary sequence" illustrates the predictions of the adopted model for main-sequence stellar masses 0.3–0.7 $M_\odot$. The YSOs, labeled in italic type, progress from class 0 protostars embedded in dense gas, with strong submillimeter emission and well-collimated outflows (VLA 1623, IRAS 03282) to class III weak-line T Tauri stars with no associated gas and little infrared excess (LkCa5, 043124).

depth below the front surface. Then the variation of $T[r_{\tau=1}]$ with b and θ is naturally divided into three ranges of b: the inner region, $0 \leq b \leq b_1$, at the base of the cone where the envelope has its maximum temperature T_1; the cone region, $b_1 \leq b \leq r_2 \sin \theta$, within the projected area of the cone, and the outer region, $r_2 \sin \theta \leq b \leq r_2$ between the outer edge of the cone and the outer radius of the sphere. The "photosphere" is then spherical with radius r_1 in the inner region, approximately conical in the cone region, and approximately spherical, with radius slightly less than r_2, in the outer region.

The temperature $T_{\rm in}[r_{\tau=1}]$ in the inner region is by definition T_1, the maximum envelope temperature. To determine the temperature $T_{\rm cone}[r_{\tau=1}]$ in the cone region we use the condition of unit optical depth, measured inward along the line of sight from the front surface of the cone:

$$\frac{T[r_{\tau=1}]}{T_1} = \left(\frac{r_1}{r_{\tau=1}}\right)^{1/2} = \left(\frac{r_1^2}{b^2 + z_{\tau=1}^2}\right)^{1/4}, \tag{35}$$

where $z_{\tau=1}$ is defined by the solution to

$$1 = \tau = \frac{\tau_{12} r_1^{1/2}}{2(1 - x^{-1/2})} \int_{z_{\tau=1}}^{b/\tan\theta} dz(b^2 + z^2)^{-3/4}. \tag{36}$$

Here τ_{12} is the optical depth from r_1 to r_2, and $x \equiv r_2/r_1$. The integral in equation (36) is an elliptic integral which cannot be simply integrated in closed form, so we use an approximation in order to enable analytic evaluation of $T_{\rm bol}$:

$$\frac{T_{\rm cone}(r_{\tau=1})}{T_1} = \frac{1 - x^{-1/2}}{\tau_{12}} \cos^2 \theta + \left(\frac{r_1 \sin \theta}{b}\right)^{1/2}. \tag{37}$$

Equation (37) is written to match equation (35) in the limits $b \ll z$, when $T_{\rm cone}[r_{\tau=1}]/T_1 \approx (1 - x^{-1/2})/\tau_{12} + (r_1 \tan \theta/b)^{1/2}$, and $b \gg z$, when $T_{\rm cone}[r_{\tau=1}]/T_1 \approx (r_1 \sin \theta/b)^{1/2}$. The coefficient $\cos^2 \theta$ is chosen to provide smooth variation with θ between

these limits. Other choices, e.g., $\cos^n \theta$, $n \neq 2$, make only slight changes in the dependence of T_{bol} on θ given later in this section. For small opening angles most of the temperature variation is with optical depth, while for large opening angles and for $b \gg z$ most of the temperature variation is with b.

In the outer region between the projected outer boundary of the cone and of the sphere, the same method of approximation as for the cone region gives

$$\frac{T_{\mathrm{out}}[r_{\tau=1}]}{T_1} = \frac{1 - x^{-1/2}}{\tau_{12}} \cos^2 \theta + x^{1/2} \ . \tag{38}$$

Note that equations (37) and (38) satisfy the requirement that they give the same temperature, $T_{\mathrm{cone}}[r_{\tau=1}] = T_{\mathrm{out}}[r_{\tau=1}]$, at the boundary $b = r_2 \sin \theta$ between the cone and outer regions. We obtain b_1, the boundary between the inner and cone regions by requiring that $T_{\mathrm{in}}[r_{\tau=1}]$ and $T_{\mathrm{cone}}[r_{\tau=1}]$ give the same value at b_1:

$$b_1 = \frac{r_1 \sin \theta}{(1 - \{[(1 - x^{-1/2}) \cos^2 \theta]/\tau_{12}\})^2} \tag{39}$$

With equations (37)–(39) we calculate $T_{\mathrm{bol}}(\theta; \phi = 0)$ from the definition of T_{bol} by taking the zeroth and first frequency moments of equation (34):

$$\frac{T_{\mathrm{bol}}}{T_1} = \frac{\displaystyle\int_0^{b_1} db\, b\{[T_{\mathrm{in}}(r_{\tau=1})]/T_1\}^5 + \int_{b_1}^{r_2 \sin \theta} db\, b\{[T_{\mathrm{cone}}(r_{\tau=1})]/T_1\}^5 + \int_{r_2 \sin \theta}^{r_2} db\, b\{[T_{\mathrm{out}}(r_{\tau=1})]/T_1\}^5}{\displaystyle\int_0^{b_1} db\, b\{[T_{\mathrm{in}}(r_{\tau=1})]/T_1\}^4 + \int_{b_1}^{r_2 \sin \theta} db\, b\{[T_{\mathrm{cone}}(r_{\tau=1})]/T_1\}^4 + \int_{r_2 \sin \theta}^{r_2} db\, b\{[T_{\mathrm{out}}(r_{\tau=1})]/T_1\}^4} \ . \tag{40}$$

To evaluate equation (40) with appropriate parameter choices we adopt $x = 100$, based on inner and outer envelope radii 100 AU and 0.05 pc, and envelope optical depths $r_{12} = 10$, 20, 30, and 40. These values of optical depth are high enough to ensure that the photospheric approximation is valid, and that the resulting values of T_{bol} lie in the range 100–600 K where the emissivity approximation $\kappa_0 = 5$ cm^2 g^{-1} is warranted. This range of T_{bol} corresponds to class I sources. These choices of τ_{12} set corresponding values of the inner envelope temperature T_1 according to equations (13) and (22). The resulting relations $T_{\mathrm{bol}}(\theta; \phi = 0)$ are shown as the heavy curves labelled "pole-on" in Figure 13.

Figure 13 shows that T_{bol} increases by a factor 2–3 as the cone opening angle θ increases from its minimum to maximum values. At its minimum ($\theta = 0$) the envelope is a sphere of inner radius r_1 and outer radius r_2; at its maximum ($\theta = 90°$) the system is essentially a disk of inner radius r_1, outer radius r_2, and thickness $2r_1$. For the range of angles $\theta = 5$ to 25 deg typical of CO outflows (Fukui et al. 1993), the range of T_{bol} is as small as 250 to 330 K for $\tau_{12} = 10$, and as large as 140 to 350 K for $\tau_{12} = 40$. In all cases the increase in T_{bol} with opening angle would not change the assignment of the spectral class from class I to class II.

We estimate $T_{\mathrm{bol}}(\theta, \phi)$ for viewing angles ϕ other than pole-on, i.e., for $0 < \phi \leq \pi/2$, by calculating $\langle T_{\mathrm{bol}} \rangle$, the average T_{bol} for a uniform distribution of orientation of the cone symmetry axis with respect to the line of sight. To simplify the analysis we take $T_{\mathrm{bol}}(\theta, \phi)$ to have one of two already calculated pole-on values. When the line of sight lies within the cone ($\phi \leq \theta$) we take $T_{\mathrm{bol}}(\theta, \phi) = T_{\mathrm{bol}}(\theta, 0)$, the pole-on value of T_{bol} for a cone of the same opening angle θ. When the line of sight lies outside the cone ($\phi > \theta$) we take $T_{\mathrm{bol}}(\theta, \phi) = T_{\mathrm{bol}}(0, 0)$, the value of T_{bol} for a sphere with "no cone," since when $\phi > \theta$ the hot emission from inside the cone is essentially invisible through the optically thick envelope which surrounds the cone. Then $\langle T_{\mathrm{bol}} \rangle$ is just the mean of these two values, weighted by the corresponding solid angles:

$$\langle T_{\mathrm{bol}} \rangle = (1 - \cos \theta) T_{\mathrm{bol}}(\theta, 0) + \sin \theta\, T_{\mathrm{bol}}(0, 0) \ . \tag{41}$$

The four fainter curves in Figure 13 show $\langle T_{\mathrm{bol}} \rangle$ for the same optical depths as the four pole-on curves of $T_{\mathrm{bol}}(\theta; \phi = 0)$. These indicate that for the range of opening angles $\theta = 0°$ to $25°$ representative of CO outflows, $\langle T_{\mathrm{bol}} \rangle$ averaged over all viewing angles is only slightly greater than the no-cone value $T_{\mathrm{bol}}(0, 0)$, by at most 20 K. Only when the opening angle exceeds about $50°$ does $\langle T_{\mathrm{bol}} \rangle$ appreciably exceed the no-cone value.

These estimates are crude, and they remain to be tested by more detailed numerical calculations. Nonetheless, they indicate that if a centrally heated spherical envelope with a conical cavity has an opening angle typical of CO outflows, and if it has a class I spectrum, its T_{bol} can increase by 100 to 200 K, or by a factor 1.3–2.5, as its viewing angle changes from outside the cone to inside the cone. Further, for typical opening angles the average T_{bol} over all viewing angles is only slightly greater than the no-cone value of T_{bol}. The variation of T_{bol} with observationally likely viewing angles is thus relatively small because the hot dust near the base of the cone generally subtends a relatively small solid angle compared to that of the cold dust in the extended envelope.

The conclusions that orientation of class I sources has relatively little effect on their spectral redness was also reached by Adams (1990) and by Chen et al. (1997). Adams (1990) computed the dependence of column density on viewing angle for a rotating collapsing envelope with density profile based on the solution of Terebey et al. (1984) and found that the column density, and thus the optical depth, varied by less than a factor of 2 for a wide range of viewing angles. Chen et al. (1997) compared T_{bol} for 24 YSOs in Taurus with their integrated intensity in the $J = 1$–0 line of C^{18}O, a measure of large-scale envelope column density. The two quantities are well correlated for class 0 and class I sources, indicating that variations in orientation do not significantly degrade the correlation between T_{bol} and column density.

Furthermore, we note that the dependence of T_{bol} on viewing angle in the models of YBL is also relatively weak, when the YBL spectra are analyzed in terms of T_{bol}. YBL show the maximum variation with viewing angle in their Figure 8, for a 10
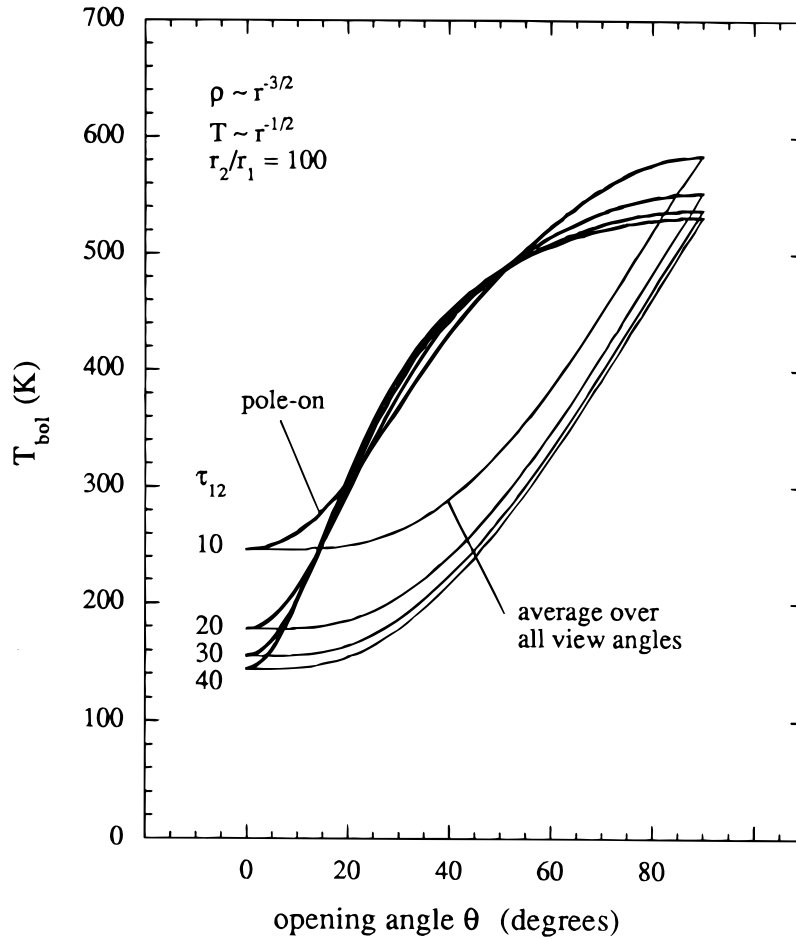
FIG. 13.—Relation of $T_{\rm bol}$ (*heavy lines*) and $\langle T_{\rm bol}\rangle$, the average $T_{\rm bol}$ over a uniform distribution of viewing angles (*light lines*), vs. cavity opening angle θ for a spherical envelope with a biconical cavity. Each curve is for a different envelope optical depth at 12 μm, $\tau_0 = 10, 20, 30$, and 40. $T_{\rm bol}$ and $\langle T_{\rm bol}\rangle$ each increase with opening angle, but for the range of opening angles associated with CO outflows ($\theta < 25°$) these increases are smaller than those due to changes in optical depth.

$M_\odot$ protostar at the greatest age in their calculations, ~ 7000 yr. Then the frequency of the infrared peak of the spectral energy distribution (νF_ν) increases by a factor 1.7 from 1.4×10^{13} Hz, as ϕ decreases from 90° to 0°. This factor of increase is comparable to that seen in $T_{\rm bol}$ in Figure 12. But for angles $\phi \leq 65°$, a second maximum due to the protostar appears at optical frequencies. In the pole-on case this optical maximum has νF_ν less than the infrared maximum by a factor of only 2.2. As YBL point out, this similar intensity of optical and infrared maxima could lead to classification of the spectrum as either class I or II, depending on the viewing angle. However, the dependence of $T_{\rm bol}$ on viewing angle is much less dramatic because $T_{\rm bol}$ is defined in terms of the mean of the spectrum (F_ν) rather than of the spectral energy distribution (νF_ν). The optical peak in the pole-on case in YBL Figure 8 would be less intense than the infrared peak by a factor of 45 in F_ν, much less than the factor 2.2 in νF_ν, and negligible in its effect on $T_{\rm bol}$. The range of $T_{\rm bol}$ corresponding to the infrared peaks in YBL Figure 8 is at most ~ 170 to 290 K, entirely within the class I range (70–650 K; Chen et al. 1995).

In contrast to the class 0 and class I sources, the class II sources should show significant variation in both $L_{\rm bol}$ and $T_{\rm bol}$ due to changing orientation of the disk axis with respect to the line of sight. Sources with significant disk emission but little overlying envelope should appear as classical T Tauri stars with a wide range of infrared excess, depending on the disk size and orientation (e.g., ALS; Kenyon et al. 1993, and references therein).

Disk orientation is difficult to measure directly, but suggestive indirect evidence exists for variation of disk orientation. Chen et al. (1995) showed that $T_{\rm bol}$ is significantly better correlated with independent estimates of YSO age for classes 0 and I (candidate protostars) and for class III (weak-line T Tauri stars) than for class II (classical T Tauri stars). Chen et al. (1997) showed that $T_{\rm bol}$ is significantly better correlated with the integrated intensity of $C^{18}O$ from the associated dense core for class 0 and I sources than for class II sources. In each case the decorrelation for class II sources was interpreted as arising from varying disk orientation.

In this paper the disk symmetry axis has been assumed to lie along the line of sight, and a detailed calculation of $L_{\rm bol}$ and $T_{\rm bol}$ for other angles, i.e., $\phi > 0$, is beyond the scope of this paper. Here we discuss qualitatively how $L_{\rm bol}$ and $T_{\rm bol}$ should change with increasing ϕ for a star-disk system with no overlying envelope. For ϕ sufficiently small, so that the disk inner edge does not occult the star, $L_{\rm bol}$ decreases and $T_{\rm bol}$ increases, both because the effective area of the disk decreases. As ϕ increases further, $L_{\rm bol}$ continues to decrease as the disk occults an increasing fraction of the stellar flux, and emits an increasing fraction of the disk luminosity in directions perpendicular to the line of sight. Now $T_{\rm bol}$ also decreases as the

reduction in stellar light becomes more important than the reduction in disk area. When $\phi = \pi/2$ so that the disk is viewed edge-on, both $L_{\rm bol}$ and $T_{\rm bol}$ should be significantly less than when $\phi = 0$ so that the disk is viewed pole-on.

As it becomes possible to measure ϕ observationally, e.g., through optical studies of jets and millimeter interferometric studies of disks, it will be important to extend the models presented here, for the optically thin approximation, when $\phi > 0$. At present, we caution against applying the current model to a classical T Tauri star such as HL Tau, which has evidence for significant obscuration by a nearly edge-on disk (Cohen 1983; Stapelfeldt et al. 1995). The model has no such restriction, and should apply, for classical T Tauri stars (class II sources) with disks which are more nearly face-on, for all other pre–main-sequence stars (classes 0, I, and III), and for main-sequence stars.

5. SUMMARY AND DISCUSSION

In this paper, we have developed the concept of the BLT diagram as a method of describing and characterizing the evolution of young stellar objects. Our results can be summarized as follows:

1. The BLT diagram provides a useful way to study the evolution of young stellar objects for all evolutionary phases of relevance for star formation. In particular, the BLT diagram can simultaneously consider both deeply embedded protostellar objects and fully revealed PMS stars.

2. We have presented a simple analytical model to calculate theoretical evolutionary tracks in the BLT diagram. Although highly idealized, these tracks provide a good representation of the evolution of young stellar objects. They should be useful for evaluating and comparing the history of star formation in well-studied complexes of young stars.

3. The tracks in the BLT diagram show a peak luminosity near a bolometric temperature of $T_{\rm bol} = 200$–600 K, in the class I period of their spectral evolution. This peak, described by equations (31) and (33), arises because the luminosity of a YSO increases during the dynamical infall phase, as its mass increases, and the luminosity decreases during the pre-main sequence phase, as it contracts at nearly fixed mass toward the main sequence.

4. The general shape of the tracks for $M_\star = 0.3, 0.5$, and $0.7\ M_\odot$ in the BLT diagram calculated from our simple model is in good agreement with the observed distribution of 254 YSOs in the nearest star-forming complexes, showing a distinct decrease in luminosity from its peak value of $L_{\rm bol} \approx 3\ L_\odot$ at $T_{\rm bol} = 250$ K to $L_{\rm bol} \approx 0.4\ L_\odot$ as $T_{\rm bol}$ increases to 3000 K.

5. The protostellar mass infall rate is modeled as decreasing gradually, rather than suddenly, in order to smoothly join the protostellar and pre–main-sequence phases. This change reduces the peak luminosity by a factor of 4 from that of a collapsing singular isothermal sphere with sudden termination of the infall, giving better agreement between predicted and observed luminosities in nearby star-forming regions.

6. The model is somewhat unrealistic in its treatment of class II T Tauri star emission because the model disk is assumed to be face-on and in some cases is smaller than expected for a centrifugally supported accretion disk. It will be important to correct these shortcomings in future treatments. Nonetheless the model tracks join smoothly between the infall and contraction phases of the YSO evolution, and match observed values of $L_{\rm bol}$ and $T_{\rm bol}$ for many class II sources.

7. If the envelope is aspherical, its orientation with respect to the line of sight changes $T_{\rm bol}$ relatively little for class 0 and class I sources. This effect is investigated with a model of a sphere with a biconical cavity. For cavity opening angles similar to those observed in CO outflows, sources with class I values of $T_{\rm bol}$ show an increase of 100–200 K from equator-on to pole-on orientations. This variation is not great enough to change the assignment of the spectral class from class I to class II. The mean $T_{\rm bol}$ over a uniform distribution of orientations is only slightly greater than the equator-on value of $T_{\rm bol}$, and this difference is much less than the change in $T_{\rm bol}$ due to changes in envelope optical depth from $\tau_{12} = 10$ to 40.

A large amount of further development work for the BLT diagram remains to be done. The theoretical model used to calculate tracks for this paper is highly idealized and can be improved in many ways. One important issue is the manner in which the infall onto protostar ends. In this present treatment, we posit a simple time dependence (eq. [25]) so that at early times the infall rate is equal to its (constant) value predicted by the SIS solution; at late times, the mass infall rate decreases exponentially. Although this *ansatz* provides a good qualitative description of the process, it is no substitute for a detailed calculation of how the infall ends. This issue, the end of infall, ultimately determines the final masses of stars and thus plays a central part in the star formation process. In this present work, we do not calculate the final mass of the star, instead, we present tracks for a given final stellar mass. In a complete theory, however, the final mass of the star should be determined for a given set of initial conditions (see, e.g., Adams & Fatuzzo 1996; Nakano, Hasegawa, & Norman 1995).

Another area for future work is to perform more accurate and detailed radiative transfer calculations to determine the bolometric temperature $T_{\rm bol}$. In this work, we have considered the simplest possible treatment of protostellar radiative transfer in order to obtain analytic results. While such results are invaluable for understanding the physical nature of the problem, detailed numerical calculations must be done in order to obtain more quantitative results (see, however, the Appendix). In particular, different dust opacity models should be used. Comparison of the results of Adams et al. 1987, Butner et al. 1991, and Kenyon et al. 1993 suggest that dust opacity is one of the most important and uncertain ingredients of the protostellar radiative transfer problem.

An important application of the BLT tracks presented in this paper will be the description of the mass and age distributions of YSOs in well-studied star-forming complexes. Such descriptions should allow us to compare for the first time the mass distribution and birth history of "recent" star formation, i.e., in the last Myr, with those of "older" star formation already known from optical studies of T Tauri stars. For example, the distribution of YSOs in Figure 11, in relation to the model lines of constant mass and time, suggest that the birthrate of low-mass stars in the nearest complexes has not been constant, but rather has decreased significantly in the last Myr, by a factor of at least ~ 3.

APPENDIX

ANALYTIC AND NUMERICAL CALCULATIONS OF BOLOMETRIC TEMPERATURE AND LUMINOSITY

In this section we compare the T_{bol} and L_{bol} predicted by a photospheric approximation of the type in § 2 with values predicted from detailed numerical models is described by Adams & Shu (1986; hereafter AS; see also Adams et al. 1987 and Adams 1990). The values agree closely, suggesting that the photospheric approximation in this paper is a good approximation to the AS models of class I sources.

The photospheric approximation is largely the same as in § 2 but is simpler because the AS models apply primarily to sources with $T_{bol} = 100-700$ K, corresponding to mean frequency $\langle v \rangle = 1-7 \times 10^{13}$ Hz, or to wavelengths 4–30 μm. For these wavelengths it is more appropriate to model the emissivity as $\kappa = \kappa_0 v^0$ than as $\kappa = Av^1$ as in § 2. Here we adopt $\kappa_0 = 5$ cm^2 g^{-1} in accordance with the emissivity curve of AS over the frequency range $1-7 \times 10^{13}$ Hz. This frequency range contains the silicate absorption features and hence the opacity profile is relatively flat in this range. This change simplifies the

TABLE 2
NUMERICAL CALCULATIONS OF T_{bol} AND L_{bol} BASED ON THE
MODELS OF ADAMS & SHU (1986)

a (km s^{-1})	Ω (10^{-14} s^{-1})	M ($M_\odot$)	$\log T_{bol}$ (K)	$\log L_{bol}$ ($L_\odot$)
0.20......	2	0.2	2.26	0.497
		0.3	2.31	0.666
		0.4	2.40	0.787
		0.5	2.51	0.883
		0.6	2.63	0.960
	3	0.2	2.24	0.491
		0.3	2.34	0.663
		0.4	2.49	0.785
		0.5	2.64	0.881
	5	0.1	2.02	0.199
		0.2	2.25	0.487
		0.3	2.46	0.660
0.35......	2	1.35	2.27	1.81
		1.40	2.28	1.82
		1.50	2.29	1.85
		1.60	2.30	1.88
		1.70	2.31	1.90
		1.80	2.32	1.93
		1.90	2.33	1.95
		2.00	2.33	1.97
	3	1.0	2.17	1.68
		1.1	2.21	1.72
0.35......	3	1.2	2.23	1.75
		1.3	2.25	1.79
		1.4	2.26	1.82
		1.5	2.27	1.85
		1.6	2.28	1.88
		1.7	2.29	1.90
		1.8	2.30	1.93
		1.9	2.32	1.95
		2.0	2.33	1.97
	10	0.5	1.96	1.37
		0.6	2.03	1.45
		0.7	2.08	1.52
		0.8	2.11	1.57
		0.9	2.16	1.62
		1.0	2.20	1.67
		1.1	2.25	1.71
		1.2	2.29	1.75

NOTE.—a, Ω, and M are, respectively, the isothermal sound speed, the initial angular frequency of rotation, and the current mass of the star-disk system. All runs presented here assume that the efficiency of mass accretion from disk to star is $\eta_D = 0.76$, and the efficiency of dissipation of stellar energy of differential rotation into heat is $\eta_\star = 1$ (see AS for further details).

photospheric approximation because now the radius r_1 of the $\tau = 1$ surface is independent of frequency. Then we may write

$$L_{\rm bol} = 4\pi\sigma r_1^2 T_{\rm bol}^4 . \tag{A1}$$

We express r_1 in terms of the collapsing singular isothermal sphere model, where isothermal gas of temperature T collapses from inside out to form a star of mass $M_\star$:

$$r_1 = \left(\frac{\kappa_0 m_0}{\pi}\right)^2 \left(\frac{kT}{2mG}\right)^3 M_\star^{-1} \tag{A2}$$

Here m_0 is the dimensionless constant 0.975 (Shu 1977), and m is the mean molecular mass, $2.33m_H$. We assume that this luminosity $L_{\rm bol}$ is due solely to $L_{\rm in}$, the luminosity from infall onto the star-disk system, given by equation (30). The infall is assumed to be early enough, i.e., $t \ll t_\star$, so that $dM_\star/dt$ is constant. To facilitate comparison with AS we adopt their modification of equation (30) to account for dissipation as material falls onto the circumstellar disk, and as it transfers from the disk to the star:

$$L_{\rm in} = \eta GM_\star(dM_\star/dt)/r_\star , \tag{A3}$$

where $\eta = (\eta_D/2)(1 + \eta_D \eta_\star)$, where η_D is the ratio of rates of mass increase from the disk onto the star and from the envelope onto the disk, and where $\eta_\star$ is the efficiency with which the star dissipates its energy of differential rotation. For the range of plausible values (see AS: $\eta_D = 0.76$ and $\eta_\star = 0, 0.5,$ or 1) the range of η is relatively small: 0.4–0.7.

Combining equations (A2) and (A3) eliminates $M_\star$, yielding

$$L_{\rm bol} = \frac{\sigma^{1/3}}{\pi} \left(\frac{\eta}{r_\star}\right)^{2/3} \left(\frac{\kappa_0 T_{\rm bol}}{2}\right)^{4/3} \left(\frac{m_0}{G}\right)^2 \left(\frac{kT_k}{m}\right)^3 , \tag{A4a}$$

$$\frac{L_{\rm bol}}{L_\odot} = 0.00167 \left(\frac{T_{\rm bol}}{\rm K}\right)^{4/3} \left(\frac{T_k}{10\ \rm K}\right)^3 , \tag{A4b}$$
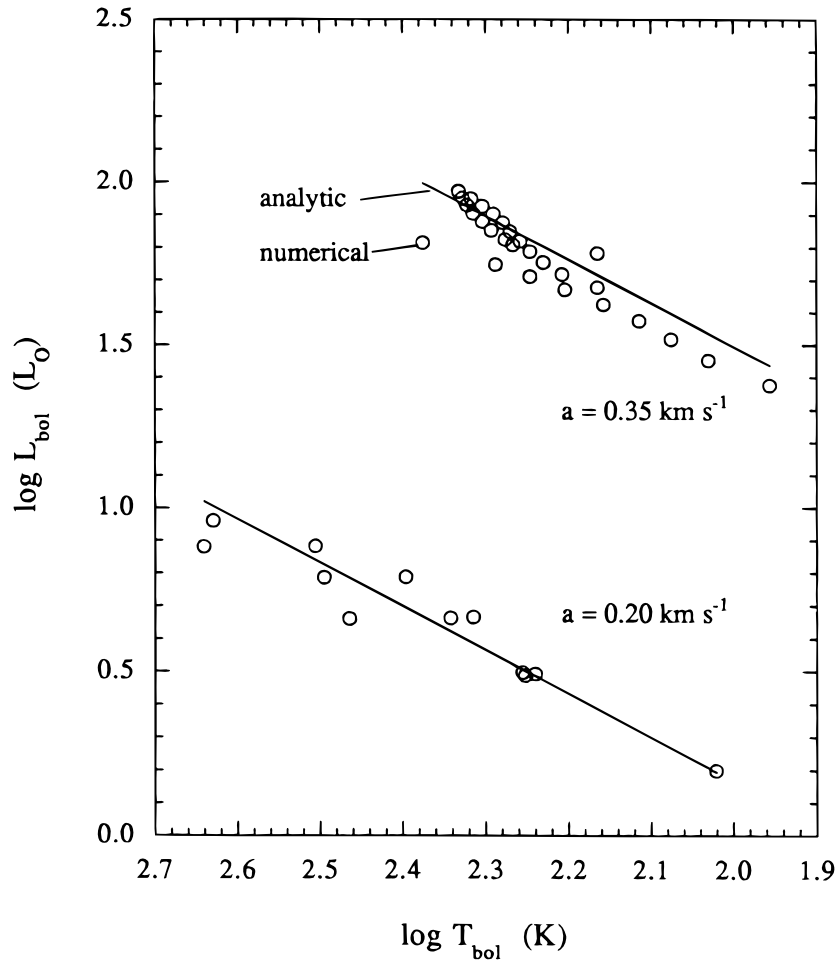

FIG. 14.—BLT diagram for numerical models of spectra from a rotating, collapsing envelope, according to the theory of Adams & Shu (1986) (*open circles*), for the parameter values in Table A1. *Solid lines* indicate the predictions of the analytic "photospheric approximation" of the same type as is used in the treatment of the optically thick envelope in § 2. The photospheric approximation fits the values from the numerical model well and fits slightly better for colder gas, with sound speed 0.20 km s^{-1}, than for warmer gas with sound speed 0.35 km s^{-1}.

where in equation (A4b) we adopt $r_\star = 3 \, R_\odot$ (Stahler 1988), $\kappa_0 = 5 \, cm^2 \, g^{-1}$ as justified above, and $\eta = 0.67$, based on $\eta_D = 0.76$ and $\eta_\star = 1.0$. Similarly, equations (A1–A3) also lead to scaling relations between L_{bol}, T_{bol}, and $M_\star$, and between L_{bol}, T_{bol}, and t, as given in Chen et al. (1995).

We compare the prediction of equation (A4b) with the output of the program of AS for the 39 cases summarized in Table 2. All of these cases represent model runs with $\eta_D = 0.76$ and with $\eta_\star = 1.0$ There are two different sound speeds, $a = 0.20$ and $0.35 \, km \, s^{-1}$, corresponding to kinetic temperatures $T_k = 11$ and 34 K. For each value of a, there are three values of the initial angular velocity Ω: 2, 3, and $5 \times 10^{-14} \, s^{-1}$, ($a = 0.20 \, km \, s^{-1}$), or 2, 3, and $10 \times 10^{-14} \, s^{-1}$, ($a = 0.35 \, km \, s^{-1}$). For each value of Ω there are 3–11 calculations of the broadband spectral emission for a particular mass M of the current star-disk system, ranging from 0.2 to 2.0 $M_\odot$. For each of these spectral calculations we computed $\log T_{bol}$ and $\log L_{bol}$ according to the usual definitions.

Figure 14 compares the relation of the photospheric approximation of $\log L_{bol}$ for a given T_{bol} in equation (A4) to the numerical calculations summarized in Table 2. The analytic values of $\log L_{bol}$ depart from the numerical values by less than 0.2 in all cases and by less than 0.1 in most cases. The agreement is slightly better for the colder gas ($a = 0.20 \, km \, s^{-1}$) than for the warmer gas ($0.34 \, km \, s^{-1}$). The variation in angular frequency makes only a slight difference in the relation between L_{bol} and T_{bol}. This suggests that the radius where rotation begins to significantly alter the optical depth is smaller than the radius r_1 where $\tau = 1$, i.e., rotational effects have little impact on T_{bol}. (On the other hand, rotation has a relatively large effect on the spectral energy distribution at wavelengths shorter than the peak, i.e., in the near infrared). The departures of analytic and numerical L_{bol} for a given T_{bol} are significantly smaller than the typical uncertainty in $\log L_{bol}$ due to photometric errors, binarity, extinction, and incomplete spectral coverage (Chen et al. 1995). Therefore we regard equation (A4) as a useful approximation to $\log L_{bol}$ and $\log T_{bol}$ based on the more detailed numerical calculations of Adams & Shu (1986) and Adams (1990).

REFERENCES

Adams, F. C. 1988, Ph.D. thesis, Univ. California, Berkeley
———. 1990, ApJ, 363, 578
———. 1991, ApJ, 382, 544
Adams, F. C., & Fatuzzo, M. 1996, ApJ, 464, 256
Adams, F. C., Lada, C. J., & Shu, F. H. 1987, ApJ, 321, 788 (ALS)
Adams, F. C., & Shu, F. H. 1985, ApJ, 296, 655
———. 1986, ApJ, 308, 836
André, P. 1995, Ap&SS, 224, 29
André, P., Ward-Thompson, D., & Barsony, M. 1993, ApJ, 406, 122
Bachiller, R. 1996, ARA&A, 34, 111
Bally, J., & Lada, C. J. 1983, ApJ, 265, 824
Beckwith, S. V., Sargent, A. I., Chini, R. S., & Guesten, R. 1990, AJ, 99, 924
Beichman, C. A., Myers, P. C., Emerson, J. P., Harris, S., Mathieu, R., Benson, P. J., & Jennings, R. E. 1986, ApJ, 307, 337
Bontemps, S., André, P., Terebey, S., & Cabrit, S. 1996, A&A, 311, 858
Butner, H. M., Evans, N. J., Lester, D. F., Levreault, R. M., & Strom, S. E. 1991, ApJ, 376, 676
Chandler, C. J., Gear, W. K., Sandell, G., Hayshi, S., Duncan, W. D., Griffin, M. J., & Hazell, A. S. 1990, MNRAS, 243, 330
Chen, H., Grenfell, T., Myers, P. C., & Hughes, J. D. 1997, ApJ, 478, 295
Chen, H., Myers, P. C., Ladd, E. F., & Wood, D. O. S. 1995, ApJ, 445, 392
Cohen, M. 1983, ApJ, 270, L69
D'Antona, F., & Mazzitelli, I. 1994, ApJS, 90, 467
Draine, B. T., & Lee, H. M. 1984, ApJ, 285, 89
Foster, P. N., & Chevalier, R. A. 1993, ApJ, 416, 303
Fukui, Y., Iwata, T., Mizuno, A., Bally, J., & Lane, A. 1993, in Protostars and Planets, Vol. 3, ed. E. Levy & J. Lunine (Tucson: Univ. Arizona Press), 603
Fuller, G. A., & Myers, P. C. 1992, ApJ, 384, 523
Greene, T. P., Wilking, B. A., André, Philippe, Young, E. T., & Lada, C. J. 1994, ApJ, 434, 614
Hartigan, P. 1993, AJ, 105, 1511
Hartmann, L. W., Calvet, N., Gullbring, E., & D'Alessio, P. 1997b, ApJ, submitted
Hartmann, L. W., Cassen, P., & Kenyon, S. J. 1997a, ApJ, 475, 770
Hayashi, C., Hoshi, R., & Sugimoto, D. 1962, Prog. Theor. Phys. Suppl., 22, 1
Henyey, L. G., LeLevier, R., & Levee, R. D. 1955, PASP, 67, 154
Hartzsprung, E. 1905, Zur Strahlung der Sterne (Z. Wiss Photog., 3)
Hughes, J. D., Hartigan, P., Krautter, J., & Kelemen, J. 1994, AJ, 108, 1071
Iben, I. 1965, ApJ, 141, 993
Kenyon, S. J., Calvet, N., & Hartman, L. 1993, ApJ, 414, 676
Kenyon, S. J., & Hartmann, L. W. 1995, ApJS, 101, 117

Kenyon, S. J., Hartmann, L. W., Strom, K. M., & Strom, S. E. 1990, AJ, 99, 869
Kenyon, S. J., Whitney, B. A., Gower, M., & Hartmann, L. 1993, ApJ, 414, 773
Königl, A., & Ruden, S. P. 1993, in Protostars and Planets, Vol. 3, ed. E. Levy & J. Lunine (Tucson: Univ. Arizona Press), 641
Lada, C. J. 1987, in IAU Symp. 115, Star Forming Regions, ed. M. Peimbert & J. Jugaku (Dordrecht: Reidel), 1
Lada, C. J., & Wilking, B. A. 1984, ApJ, 287, 610
Ladd, E. F., Adams, F. C., Casey, S., Davidson, J. A., Fuller, G. A., Harper, D. A., Myers, P. C., & Padman, R. 1991, ApJ, 366, 203
Levee, R. D. 1953, ApJ, 117, 200
Lynden-Bell, D., & Pringle, J. E. 1974, MNRAS, 168, 603
Mardones, D., Myers, P. C., Tafalla, M., Wilner, D. J., Bachiller, R., & Garay, G. 1997, ApJ, 489, 721
Mercer-Smith, J., Cameron, A. G. W., & Epstein, R. L. 1984, ApJ, 279, 363
Mouschovias, T. 1987, in Physical Processes in Interstellar Clouds, ed. G. Morfill & M. Scholer (Dordrecht: Reidel), 453
Myers, P. C., Fuller, G. A., Mathieu, R. D., Beichman, C. A., Benson, P. J., Schild, R. E., & Emerson, J. P. 1987, ApJ, 319, 340
Myers, P. C., & Ladd, E. F. 1993, ApJ, 413, L47 (ML)
Myers, P. C., Ladd, E. F., & Fuller, G. A. 1991, ApJ, 366, L203 (MLF)
Nakano, T., Hasegawa, T., & Norman, C. 1995, ApJ, 450, 183
Natta, A. 1993, ApJ, 412, 761
Russell, H. N. 1914, Pop. Astron., 22, 275, 321
Saraceno, P., André, P., Ceccarelli, C., Griffin, M., & Molinari, S. 1996, A&A, 309, 827
Saraceno, P., D'Antona, F., Palla, F., Griffin, M., & Tommasi, E. 1996, in ESO Workshop on the Role of Dust in Star Formation, ed. H. U. Kaeufe & R. Siebenmorgen (Berlin: Springer)
Schwarzschild, M. 1958, Structure and Evolution of the Stars (Princeton: Princeton Univ. Press)
Shu, F. H. 1977, ApJ, 214, 488
Shu, F. H., Lizano, S. P., & Najita, J. 1994, ApJ, 429, 797
Stahler, S. W. 1983, ApJ, 274, 822
———. 1988, ApJ, 332, 804
Stapelfeldt, K. R., et al. 1995, ApJ, 449, 888
Terebey, S., Shu, F. H., & Cassen, P. 1984, ApJ, 286, 529
Terebey, S., Vogel, S. N., & Myers, P. C. 1992, ApJ, 390, 181
Vilas-Boas, J. S., Myers, P. C., & Fuller, G. A. 1994, ApJ, 433, 96
Wu, Y., Huang, M., & He, J. 1996, A&AS, 115, 283
Yorke, H., Bodenheimer, P., & Laughlin, G. 1995, ApJ, 443, 199 (YBL)